A global model of cometary tail disconnection events triggered by solar wind magnetic variations

Ying-Dong Jia,[1] Michael R. Combi,[1] Kenneth C. Hansen,[1] and Tamas I. Gombosi[1]

Received 14 November 2006; revised 26 February 2007; accepted 9 March 2007; published 26 May 2007.

[1] Presented in this paper are the results of a time-dependent, fully three-dimensional self-consistent ideal magneto-hydrodynamics (MHD) model of disconnection events (DEs) in the cometary plasma tail. Understanding the interaction of cometary plasma with the solar wind is a very important problem in space plasma physics. This study focuses on the detailed MHD processes which occur during DEs based on typical comets with ideal solar wind conditions, as well as different experiences of DEs triggered by different forms of heliospheric current sheet (HCS). The crossing process against a typical HCS, which is interpreted as various tangential discontinuities (TDs), is simulated. Tail rays and/or disconnected tails are formed in such simulations. With our line-of-sight integration results, we conclude that observers from different directions relative to the IMF plane will see two different types of DE image series. The magnetic reconnection that occurs in our results confirms previous publications from different models. With additional cases, our study also provides the limitation for such DEs to be triggered: the angle of magnetic field rotation across the TD should be within 90° to 270°. The effects of various intervals of multiple HCS crossings are explored to show that a 2-h minimum interval is needed for consecutive multiple HCS to trigger a DE. In addition, such DEs caused by multiple HCS crossings have more tail rays and appear closer to observations than those resulted by single HCS crossings. In addition to presenting the first global DE time evolution with a well-resolved contact-surface, our results are compared morphologically with observational images. Quasi-quantitative agreement with observational measurements is found by investigating the recession speed during the DE. Moreover, the importance of having a solar wind condition being able to trigger a frontside magnetic reconnection is found critical for such DEs to originate. The importance of a well-resolved contact surface to this problem is discussed regarding to the mass loading effect. On the basis of our deductions and simulations, an empirical equation and data table to estimate the minimum upwind boundary distance is derived with respect to the shock distance, which is sensitive to the cometary production rate.

Citation: Jia, Y.-D., M. R. Combi, K. C. Hansen, and T. I. Gombosi (2007), A global model of cometary tail disconnection events triggered by solar wind magnetic variations, *J. Geophys. Res.*, *112*, A05223, doi:10.1029/2006JA012175.

1. Introduction

[2] Both the interplanetary magnetic field (IMF) and the solar wind are highly variable in time and space. Since the discovery of the solar wind by *Biermann* [1951], attempts have been made to utilize tail appearances of comets as real-time solar wind probes [*Niedner and Brandt*, 1978; *Niedner*, 1982]. Among cometary tails the plasma tail, which is usually strait and narrow, is understood to be shaped by both the solar wind flow field and the IMF. For this reason, better knowledge of the plasma tail will provide us more information of the solar wind, which is usually not measured except in some limited regions clustered around the earth or certain interplanetary spacecraft.

[3] The most remarkable time-variable phenomenon that occurs in the plasma tail is the disconnection event (DE), in which the entire plasma tail is uprooted from the comet's head while a new tail appears and starts to grow. Such a phenomenon is first studied by the turn of twentieth century as summarized by *Barnard* [1920]. Extensive DE study can be traced back for more than 30 years [*Niedner and Brandt*, 1978]. Model simulation of DEs started to appear in the 1980s, encouraged by a couple of comet flybys which made available in situ plasma data of the inner coma [*Keitch*, 1986]. Equipped with time variable images of DEs, and based on the high dependency on both plasma and magnetic conditions in the solar wind, DE studies can be quite promising in reproducing the overall solar wind plasma and IMF configuration at certain time periods.

[1]Space Physics Research Laboratory, University of Michigan, Ann Arbor, Michigan, USA.

0148-0227/07/2006JA012175

[4] In the works of *Brandt* [1982] and *Brandt and Chapman* [2004], four different phases for DEs are named which is referred as the ''Niedner-Brandt'' sequence. In phase I the tail becomes narrower than usual, and tail rays can be observed. In phase II the tail is uprooted from the nucleus. In phase III the old tail recedes from the nucleus and a new tail forms. In phase IV the old tail disappears and the comet returns to normal.

[5] Previous studies have proposed a few theories relating DEs to the variations in solar wind conditions. Several magneto-hydrodynamics (MHD) models have been used to simulate such real-time interactions. *Schmidt-Voigt* [1989] studied the effect of both a field reversal and a 90°-field rotation but the DE was only found with a 90°-field rotation. This was later negated by *Wegmann* [2000]. *Ogino et al.* [1986] found frontside reconnections and tail reconnections induced by a field reversal using a two-dimensional MHD simulation. *Russell et al.* [1986] compared DEs with substorms and tried to relate fluid dynamic reasons to such events.

[6] Later on, two major groups of researchers have held their positions debating the cause of DEs. *Rauer et al.* [1995] and *Wegmann* [1995] updated the *Schmidt-Voigt* [1989] model and suggested that abrupt discontinuities in solar wind flow field will cause DEs. During the interaction process, there are usually two key features: first, the discontinuity interface bends over the comet nucleus forming ''isochrones'', second, the DEs are usually accompanied with shifts in tail directions. Multiple dynamic factors, such as velocity discontinuities, are shown to be causes of such DEs. *Wegmann et al.* [1996] successfully compared their model result with the observation of comet Austin whose multiple tail rays are not followed by any tail disconnection and asserted that this should be the result of a 90°-field rotation in the IMF. Unfortunately, their simulation results only show how a 90°-field rotation will trigger tail rays without tail disconnections. Whether a HCS crossing with a 180°-field reversal can create a DE is not shown. On the basis of this result, as long as the belief that DEs are always accompanied with tail direction shifts, they proposed that changes in the interplanetary magnetic field (IMF) itself will at most cause tail rays but not DEs. In their follow-up work of *Wegmann* [2000], a DE caused by a 180° rotation is studied but magnetic reconnection is denied because of the low resolution of the numerical code used. However, *Wegmann* [2000] does agree that the resulting plasmoid in the tail is the strongest for the 180° IMF rotations, compared to other amounts of field rotation.

[7] A different approach was adopted by *Yi et al.* [1994a, 1994b] and *Brandt et al.* [1999]. The heliospheric current sheet (HCS) crossings are proposed to be the reasons of most DEs, based on a collection of DE images and statistical relationships between the HCS and these DEs. In the works of *Niedner and Brandt* [1978], the idea of HCS caused DEs is first introduced while frontside reconnection is found responsible. *Niedner and Brandt* [1979] solved the ambiguity over that time by concluding that HCS crossings instead of high-speed streams are causes for DEs. *Voelzke and Matsuura* [2000] and *Voelzke* [2002] collected 19 DEs between 1985 and 1986 to study the IMP data at the time of their onsets. Most DEs in their study are not associated with a significant jump in dynamic pressure. This argument implies the HCS is a better candidate to trigger DEs than interplanetary shocks.

[8] In the three-dimensional numerical simulations of *Yi et al.* [1996], the evolution of DEs is studied extensively as an effect of frontside magnetic reconnection caused by IMF reversal. In their time-dependent MHD models, the HCS is represented by a tangential discontinuity embedded in the solar wind. Rather than the 90°-field rotation studied by the Wegmann group, the magnetic field is reversed across this discontinuity. By presenting three-dimensional density isosurface plots, and the time series of frontside magnetic reconnections, they concluded that it is the change in IMF that triggered DEs in comet plasma tail. However, the displacement of a disconnected tail can never be reproduced in such HCS crossing simulations. Such tail displacements should be caused by reasons other than an ideal IMF discontinuity. On the other hand, *Brandt and Snow* [2000] and *Snow et al.* [2004] have been engaged in searching for more observational evidences for such HCS crossings.

[9] An extensive study about the magnetic reconnections during such DEs has been carried out by two-dimensional simulations of *Ogino et al.* [1986] and *Konz et al.* [2004]. Both models have found constant tail reconnection during steady solar wind condition. *Konz et al.* [2004] have examined time evolution of current density and field strength using their plasma-neutral gas model. The morphology as well as the dayside magnetic diffusion and nightside magnetic reconnection is discussed thereafter. However, as has been discussed by *Yi et al.* [1996], a full three-dimensional simulation is necessary to explore what is inherently a three-dimensional problem and to show what line-of-sight integrated synthetic images look like. A summarizing review of the previous works mentioned above can be found in the paper by *Voelzke* [2005].

[10] Compared with the previous simulations addressed above, our study is the first self-consistent three-dimensional approach to resolve the cometary plasma environment at both the contact-surface scale and the bow shock scale and to elucidate the triggering processes for such HCS related DEs to start. In our block-based Godunov type conservative scheme with second order accuracy, no artificial resistivity is added. The only deviation of our model from ideal MHD is the source terms implementing the mass loading effect. Among the three-dimensional models used for past DE studies, the closest approach is the model of *Yi et al.* [1996], which has a lower resolution. In this work our case 1 is a reproduction of the result of the study of *Yi et al.* [1996] with a hundred times higher resolution and more details focused on the contact surface region.

[11] For Halley-sized comets, DEs are viewable around comet distances of 0.6 to 16×10^6 km in typical ground-based images [*Niedner and Brandt*, 1978; *Brosius et al.*, 1987; *Brandt et al.*, 1999]. Limited by calculation resources, we are not studying recession processes beyond 4×10^6 km with high resolution. Most of our DE phases are shown in the range of $+0.2 \times 10^6$ km upstream to -4×10^6 km downstream of the comet. The evolution processes of the disconnected tail beyond this region are presented in observed images [*Voelzke and Matsuura*, 1998; *Snow et al.*, 2004]. Nevertheless, our simulation results are the first to

provide a realistic portrayal of the temporal progression of recession that is comparable to observational measurements.

[12] In the vicinity of the solar surface, as the complex magnetic field structure in the photosphere propagates outward, it becomes simpler while its heliocentric distance increases. At about 2.5 solar radii, a single neutral sheet called the HCS is formed. This neutral sheet is a boundary that separates the two polarities drawn out by the radially accelerating solar wind. The two polarities of field can be classified into two regions. The magnetic field in these two regions points either outward or inward, respectively. As a consequence of solar rotation, the HCS usually wobbles about both sides of the ecliptic plane, while the two regions lie north and south of the HCS.

[13] The shape of the current sheet usually evolves slowly, with a typical timescale longer than a month. However, the base of the sheet in the solar photosphere close to the equator takes 27 days to complete one rotation, and the rest of sheet rotates with an angular speed almost the same. Such a rotation leads to an azimuthal velocity of about 400 km/s at 1 AU, which is close to the typical solar wind bulk speed. The orbital motion of a comet is usually ten times smaller. Even for cases in which the comet movement is not negligible, rotation of the coordinate system can still change the problem into a similar situation as we present here. Such a simplification makes the coordinate system dependent on, and only on, the upwind flow vector and the magnetic field vector. In addition to the 27-day rotation, other factors like the 7.5°-tilted dipole axis, the 11-year reversal period of the dipole polarity, as well as some dynamic effects operating in the interplanetary medium, can also contribute to the distortion of the HCS. The heliospheric latitude of the HCS can vary from 0° to as high as 78°, while the maximum latitude of the HCS can be 20° at solar minimum and over 70° at solar maximum [i.e., *Forsyth et al.*, 1997; *Smith et al.*, 2001].

[14] For a typical comet near its perihelion (within 1 AU), DEs can usually be captured by observers several times a month [*Brandt et al.*, 1999]. This appearance is associated with the transient and curved features in the HCS close to the ecliptical plane. More observational evidence is summarized by *Snow et al.* [2004].

[15] In this study, we start with a brief description of our model in section 2, followed by simulation results in section 3, which presents the detailed effect of propagating magnetic discontinuities in the solar wind on cometary plasma tails. In reality, multiple HCS crossings in a short period of time are also quite possible. On the basis of this, we discuss the period of time this field reversal needs to last in order to trigger an observable DE. Another effect of such multiple HCS crossings is multiple tail rays, which is also investigated. Moreover, we will show our simulation result of the interaction between a comet and a 90° IMF rotation, to compare with the result of *Rauer et al.* [1995] and show the importance of the magnetic field in such DEs. In section 4, to compare with the observations, we measure the recession speed and compared with previous measurements from DE images. In Appendix B, the importance for our high resolution at the contact-surface scale is discussed. As a by-product, the appropriate location of upwind boundary is estimated and a table is provided for comets with different production rates.

2. Model and Simulation Details

[16] The interaction between the solar wind and the comet is characterized by a complex system involving the super-Alfvenic solar wind plasma flow, the interplanetary magnetic field (IMF), the condensed cometary plasma, the cometary neutral particles, and the cometary dust. Two sources of plasma are considered here. In our ideal MHD model, the solar wind magnetized plasma will encounter the comet's neutral coma which is in turn ionized to become the cometary plasma [*Combi et al.*, 2004]. Reactions such as mass loading by ionization, charge exchange, recombination, and friction with the neutral coma are considered. Different from nearly all the previous studies, our full three-dimensional multiscale MHD model is capable of studying both the bow shock and the contact-surface region in high resolution simultaneously.

2.1. Three-Dimensional Block Adaptive Tree Solar Wind Roe Upwind Scheme

[17] All the simulations performed in this work utilize the block adaptive tree solar wind roe upwind scheme (BATS-R-US) code developed at the University of Michigan. BATS-R-US solves the conservative MHD equations mentioned above, based on a finite volume discretization. The block-based adaptive octree data structure allows resolution of multiple solution scales. Solution refinement is based on the scale of the local physics. As a result, the highly resolved numerical system limits the numerical resistivity to a fairly low level [*Powell et al.*, 1999; *Tóth et al.*, 2005].

[18] Our model solves the following set of normalized ideal MHD equations [*Gombosi et al.*, 1996]:

$$\frac{\partial \mathbf{W}}{\partial t} + \{\nabla \cdot \mathbf{F}\}^T = \mathbf{P} - \mathbf{L} \tag{1}$$

The state vector **W**, flux tensor **F** in equation (1) are defined as

$$\mathbf{W} = \begin{pmatrix} \rho \\ \rho \mathbf{u} \\ \mathbf{B} \\ \varepsilon \end{pmatrix} \tag{2a}$$

$$\mathbf{F} = \begin{pmatrix} \rho \mathbf{u} \\ \rho \mathbf{u}\mathbf{u} + (\mathrm{p} + \frac{1}{2}B^2)\mathbf{I} - \mathbf{B}\mathbf{B} \\ \mathbf{u}\mathbf{B} - \mathbf{B}\mathbf{u} \\ \mathbf{u}(\varepsilon + \mathrm{p} + \frac{1}{2}(\mathbf{B}\cdot\mathbf{B})) - (\mathbf{B}\cdot\mathbf{u})\mathbf{B} \end{pmatrix}^T, \tag{2b}$$

where ρ is the density, **u** and **B** are the velocity and magnetic field vectors. The total energy density ε is defined as:

$$\varepsilon = \frac{1}{2}[\rho \mathbf{u}\cdot\mathbf{u} + \frac{2p}{\gamma - 1} + \mathbf{B}\cdot\mathbf{B}], \tag{3}$$

where p is the thermal pressure. The right hand side of the equation is composed of production (**P**) and loss (**L**) source terms for mass, momentum, and energy added into the fluid.

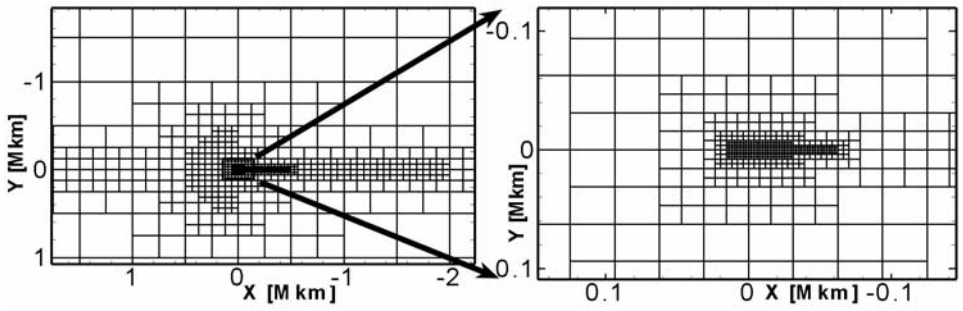

Figure 1. The multiscale block system designed with respect to the physical gradient conditions. Each block shown here contains 8 × 8 × 8 cells (not shown). The plot to the right is the enlarged view of the rectangular region in the center of left plot.

[19] In the present model, ionization-induced mass loading (photoionization, electron impact ionization, and charge exchange) and ion-neutral friction (mostly because of charge exchange) are included in the production terms:

$$\mathbf{P} = \begin{pmatrix} S \\ S\mathbf{u}_n + \eta\rho(\mathbf{u}_n - \mathbf{u}) \\ \mathbf{0} \\ \frac{1}{2}(Su_n^2 + \eta\rho(u_n^2 - u^2) - 3\eta p \end{pmatrix} \quad (4)$$

Here $\mathbf{u}_n$ is the normalized cometary neutral expansion velocity, while the mass production rate S and the ion-neutral collision rate η are defined as:

$$S = m_c f_i n_n \quad (5)$$

$$\eta = k_{in} n_n \quad (6)$$

[20] In the equations above, $n_n = \frac{Qe^{-r/\lambda_\infty}}{4\pi u_n r^2}$ is the spherical symmetric neutral density distribution function, f_i is the ionization rate, $\lambda_\infty = \frac{u_n}{f_i}$ is the ionization length, k_{in} is the ion-neutral momentum transfer collision rate, m_c is the average mass of cometary ions, which is usually estimated by a few observationally averaged values, and Q is the total neutral gas production rate of the comet. In our model, η is modified as stated in Appendix A.

[21] The loss term is associated with recombination of ions with thermal electrons. This process is described with the following loss vector:

$$\mathbf{L} = L_e \begin{pmatrix} \rho \\ \rho\mathbf{u} \\ \mathbf{0} \\ \frac{1}{2}\rho u^2 + \frac{3}{2}p \end{pmatrix} \quad (7)$$

where L_e is given by:

$$L_e = \alpha(T_e) n_e \quad (8)$$

Here $\alpha(T_e)$ is the recombination rate, while T_e and n_e are the electron temperature and density, respectively. We adopt the following form of $\alpha(T_e)$:

$$\alpha(T_e) = \begin{cases} \alpha_0 \times \sqrt{\frac{300}{T_e}} & T_e \le 200\,\mathrm{K} \\ 2.342 \times \alpha_0 T_e^{(0.2553 - 0.1633 \log T_e)} & T_e > 200\,\mathrm{K} \end{cases} \quad (9)$$

[22] The recombination rate explicitly depends on the electron density and temperature. In our simulations electron temperature is adopted from external assumptions. For example, for comet P/Halley, we use a T_e profile determined from observations [*Gombosi et al.*, 1996]. For other comet models with no observations, an assumption like $T_e = T_i = \frac{p}{2n_i k}$ could be used [*Gombosi et al.*, 1997]. In this work we adopt the latter for the electron temperature.

2.2. Grid System

[23] In order to interpret HCS crossings, and to relate them to models of solar wind-comet plasma interactions, it is essential to simulate the entire domain with enough resolution to resolve the HCS, the tail, the magnetic cavity as well as the mass-loaded shock while including the global system. BATS-R-US is quite capable of handling such problems with multiple levels of resolution changes. We use 16 levels of resolution difference in this series of simulations, which means, the largest computational cell is over 10^4 times larger than the smallest ones. Close to the nucleus, a resolution of a few kilometers is used, while far from the nucleus in the solar wind, a resolution of 10^5 kilometers is used. An example of multiple levels of grid systems is shown in a two-dimensional cut in Figure 1. In order to capture the different shapes of sharp boundaries such as shock and contact surface, a series of rectangular blocks are refined to resolve these specific structures, especially the bow shock, the tail, and the contact surface. Shown in Figure 1 is the multiscale block-based grid system we used in our time dependent runs. The plate on the left is about one-fifth of our calculation domain on each dimension, while the plate on the right is an enlarged view of the black box in the center of the left plate. The grids shown in both plates are block units. Each block unit, which looks like a square in Figure 1, contains 8 × 8 × 8 uniform cells (not shown).

[24] The coordinate system is chosen so that the sun-comet line is the x axis, where positive x points to the sun and the origin is at the comet nucleus. The z axis is the normal to the ecliptic plane pointing northward, while the y axis is placed inside the ecliptic plane to complete the right hand coordinate system.

[25] According to *Gombosi et al.* [1996], the significant mass loading of cometary ions into the solar wind extends to several ionization distances (λ_∞) in front of the comet nucleus far ahead of the bow shock. Our calculation domain

Table 1. Physical Parameters Used for the Simulations

Quantity	Symbol	Value	Units
Radius of Comet Nucleus	R_n	10	km
Gas Molecule Production Rate	Q	7.0×10^{29}	s^{-1}
Neutral Gas Speed	u_n	1	km s^{-1}
Ionization Scale Length	λ_∞	10^6	km
Ion-Neutral Momentum Transfer Collision Rate	k_{in}	1.7×10^{-9}	$cm^3 s^{-1}$
Solar Wind Number Density	n_{sw}	10	cm^{-3}
Mean Molecular Mass in Solar Wind	m_{sw}	1	amu
Solar Wind Temperature	T_{sw}	10^5	K
Solar Wind Speed	u_{sw}	400	km s^{-1}
Interplanetary Magnetic Filed (IMF) Magnitude	B_∞	3.4	nT
Mean Molecular Mass of Cometary Ions	m_c	17	amu

ranges from 16 λ_∞ ahead of the comet nucleus in the solar wind to $-48\lambda_\infty$ behind the comet in the tail direction. Numerical tests and deductions in Appendix B verify that this size of domain is sufficient for over 99% of mass loading to be included.

2.3. Initial and Boundary Conditions

[26] A typical DE lasts for less than 2 days. Over this timescale, we are going to assume that there are no significant cometary ion production rate variations. We assume that there are no significant velocity changes in the solar wind during a DE. To be comparable with most of the typical observed bright comet images, we start our simulation with a general Halley class comet orbiting close to the ecliptic plane, at a heliocentric distance of 1 AU. Based on these assumptions, the following physical parameters are summarized in Table 1.

[27] We start our study with the simplest HCS model, which is a tangential discontinuity (TD) in the solar wind. The IMF is rotated by 180° across the TD. The solar wind flow and IMF lie in the *x*-*y* plane. With our advanced grid system, both the HCS and the comet contact surface are resolved in the same global model.

[28] We model the interaction between the comet and the HCS as the interaction of two steady state MHD structures propagating one into another with the magnetized plasma flow field. Figures 2a and 2b show the slice in the ecliptic plane (IMF plane) of a steady state comet, which is used as the initial condition for our time-dependent simulations. Shown in Figure 2a is a plot of the color contours of density levels, with black lines and arrows showing the draped field lines projected into this plane. From Figure 2a we can see the location of a mass-loaded weak bow shock is marked by a sudden increase in the density, while the subsolar point of this bow shock lies around $x = 3 \times 10^5$ km. Figure 2b zooms into the region around the contact surface. The color contour is magnetic field strength, while the black lines with arrows show the projected magnetic field directions. The sudden drop in field strength around the blue region, with a subsolar point measures $x = 3 \times 10^3$ km, marks the boundary of contact surface. The stretched thin blue region in the nightside shows the position of the tail current sheet. Comet ions are compressed by solar wind ram pressure into this region to form strong currents.

[29] Shown in Figure 2c is the density contour in the meridional plane (*x*-*z* plane). The tail would look thicker but less bright from this *Y* direction than from the *Z* direction. This difference has been discussed in a previous study by *Russell et al.* [1989], and later confirmed by *Yi et al.* [1996]. The small elliptical region whose density is larger than its

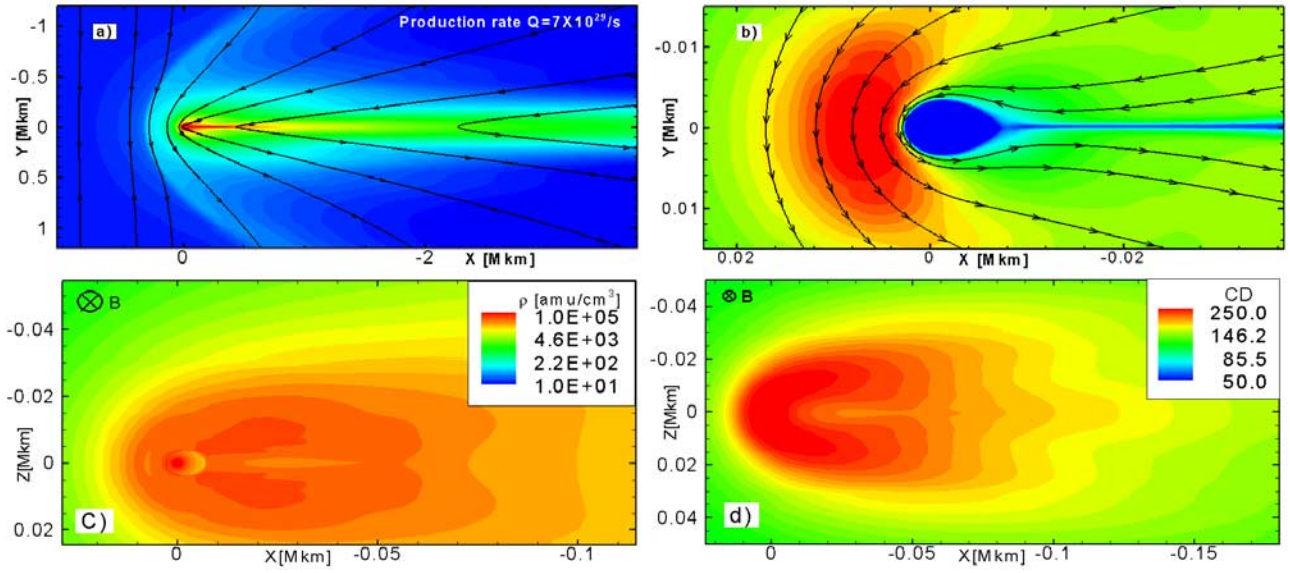

Figure 2. A steady state comet interacting with the solar wind. Magnetic field lines are projected into the *x*-*y* plane and shown in black lines. (a) Density contour showing the position of a mass-loaded bow shock. (b) Magnetic field strength contours in the ecliptic plane showing the structure of the contact surface. (c) Density contours in the meridianal plane showing the structure of the contact surface and thick tail. The IMF direction points perpendicular to this plane. (d) Column density contours in the meridianal plane showing the broad tail.

Table 2. Physical Conditions in Four Simulation Cases

	Description	IMF Jump Across HCS
Case 1	Single HCS crossing	$(0, B_\infty, 0) \rightarrow (0, -B_\infty, 0)$
Case 2	90° TD in HCS	$(0, B_\infty, 0) \rightarrow (0, 0, B_\infty)$
Case 3	Effect of large B_x component	$(B_x, B_\infty, 0) \rightarrow (-B_x, -B_\infty, 0)$
Case 4	Two HCS crossings with 2-h interval	$(0, B_\infty, 0) \rightarrow (0, -B_\infty, 0) \rightarrow (0, B_\infty, 0)$

vicinity circling around the nucleus marks the boundary of the contact surface, while the two broad wings in the nightside mark the location of plasma tail. To give a more realistic view in this direction, Figure 2d shows the ion column density measured along the y axis. It is noteworthy that the head of the comet appears to be smaller than the width of the tail. This could be difficult to see in observational images because in most images, the dust coma is not only much larger than the plasma coma, but also much brighter.

3. Results

[30] Our simulation results of typical current sheet configurations are presented in four cases in this section with extensive investigations to demonstrate the magnetic induced effects of discontinuities in the solar wind on the cometary plasma. These cases are summarized in Table 2.

3.1. Case 1, Single Ideal HCS Crossing

[31] The principal feature of a HCS is the reversal of the magnetic field. Without changing other parameters, this field reversal in the plasma is a typical stable interface classified as a tangential discontinuity (TD). As the first step, the effect of this propagating current sheet on a general Halley type comet is investigated.

[32] The typical thickness of the current sheet varies from around 10^4 to 10^5 km [*Villante amd Bruno*, 1982]. Restricted by our current resolution level in the upwind solar wind, we use 10^5 km for the HCS thickness, which is not changing during the HCS propagation before it is perturbed by the cometary plasma. In our model, this HCS is represented by a TD, in which the jump in B_y from positive to negative is the only difference between the two sides of the discontinuity. That is, the discontinuity is a jump from $\mathbf{B_1} = (0, B_\infty, 0)$ to $\mathbf{B_2} = (0, -B_\infty, 0)$. For simplicity, the propagation speed of this HCS is set as the same as the solar wind speed. Detailed results of this simulation case are shown in both two-dimensional cuts and line-of-sight integrated plots.

[33] With our grid system assigning enough resolution to locations with sharp changes in physical parameters, the processes happening to the cometary plasma environment around the nucleus throughout a DE can be observed. The TD does not change much when it encounters the bow shock because the ram pressure is still the dominant pressure balance across the bow shock, and there is no dynamical variation in our TD model. The interaction only becomes obvious when the TD propagates to locations close to the contact surface. In this region the IMF is significantly compressed by the cometary pick up ions. In regions further out from the x axis, the IMF is less compressed by the cometary obstacle. The ram pressure in general will force the magnetic field lines to bend over into a draped structure. Such compression driven by the constant solar wind flow will induce a strong current system in the dense cometary ion environment around the nucleus. The peak of this current system forms a draped shell around the nucleus, which is called the contact surface. As can be seen from Figure 2b, the magnetic field in front of this contact surface is quite strong and the field lines are highly bent. This balanced structure stores a large amount of energy, which may be released when the field reconnects. The plasma bulk flow is slowed down in this region right in front of the contact surface, forming a region with high plasma density and pressure. When a TD propagates to this region, the reversed field lines will start to reconnect as the incoming current sheet is compressed thinner and thinner. Such a reconnection will be the trigger of a DE, by suddenly moving a large amount of plasma toward the nightside.

[34] Figure 3 shows different stages of the DE, drawn in two-dimensional slices in the IMF plane (Figures 3a–3c), and the perpendicular plane (Figures 3d), in accordance with the four-stage "Niedner-Brandt" sequence. The figures focus on the region around the contact surface because the bow shock position does not change much during this whole process. All color plots are density contours, while the black lines are the magnetic field lines projected into the IMF (x-y) plane. Although different from what is observed by ground based telescopes which show the column density integrated along the line of sight, these slices are much clearer in telling us how the disconnection process occurs around the contact surface. Observability of DEs is addressed by column density plots in different viewing geometries below. The time marked on the upper left corner of each plot shows the physical time elapsed since start of the simulation when the TD is 1.6×10^7 km from the comet nucleus. The format of the numbers is in hour: minute: second.

[35] Figure 3a shows the emergence of tail rays, which corresponds to the "Niedner-Brandt" DE phase I. In the left panel around $T = 16$ h, the cometary plasma as an obstacle is compressing the incoming current sheet to be thinner and thinner. As a result of this compression (compared to Figures 2b and 2c), the size of the contact surface is decreased almost by half. Frontside magnetic reconnection starts when the incoming current sheet is too thin to sustain the strong field on both sides. Magnetic reconnection takes place in the region where the density and pressure peaks outside the magnetic cavity. As shown in Figures 2b and 2c, this is the region where a large amount of plasma population and energy are stored. It is this coincidence that helps the magnetic reconnection to effectively move a large amount of plasma into the tail. Frontside reconnections during a DE are also discussed in previous MHD results with less grid resolution, where the corresponding resistivity and magnetic diffusion are presented [*Yi et al.*, 1996; *Konz et al.*, 2004]. At this moment in Figure 3a, the HCS has not yet propagated to the tail, so the thin high density sheet in the tail still represents the steady state tail density distribution. In the thin layer outside the cavity ($-8 \times 10^3 > x > -4 \times 10^4$,

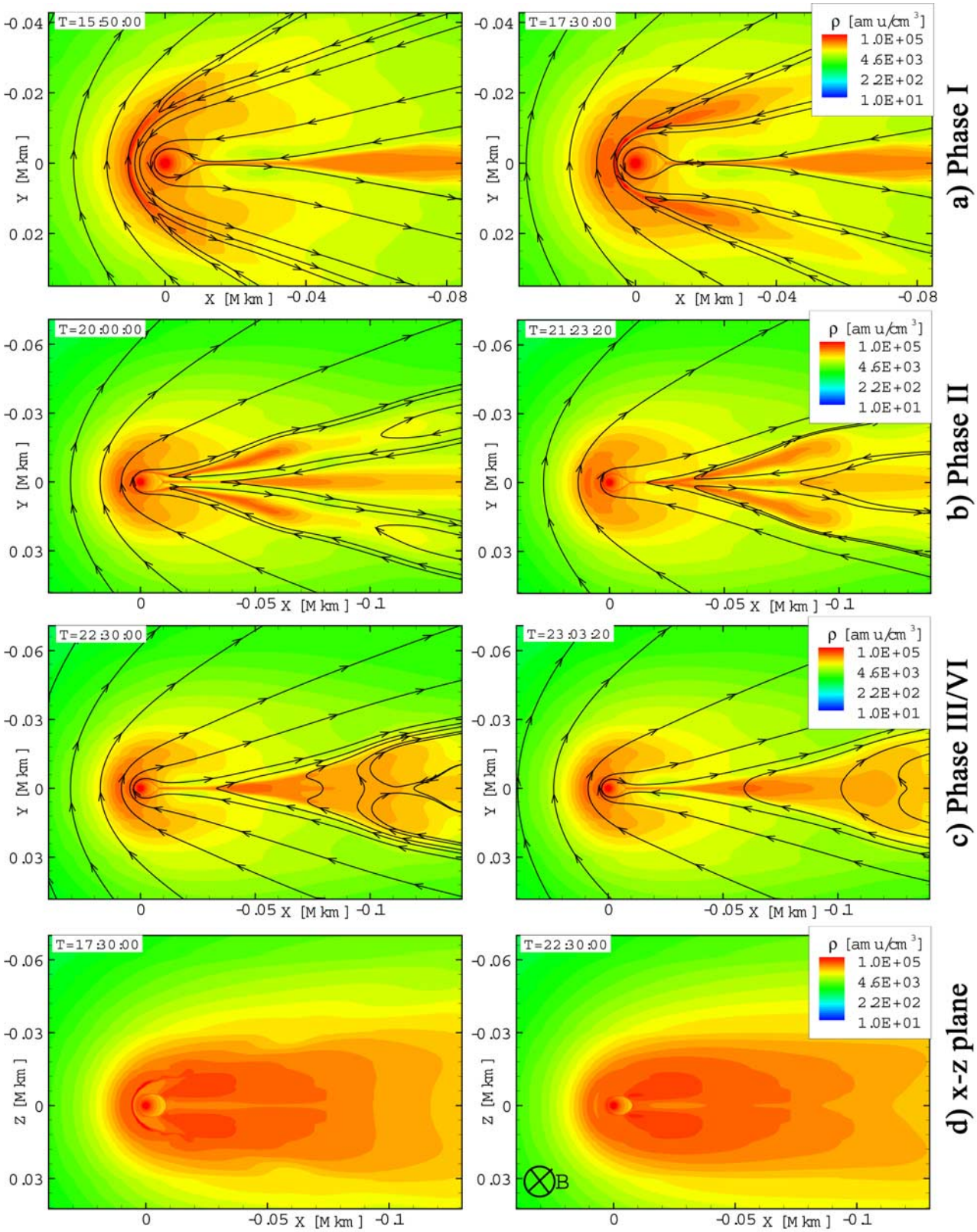

Figure 3. Density color contours with field lines projected in the IMF plane from case 1 result. (a) Phase I, tail rays: magnetic reconnection process happening in the dayside. (b) Phase II, tail disconnection: magnetic reconnection process happening in the nightside, compressing the tail. (c) Phase III/IV, old tail recedes while new tail forms: the folding process of tail rays onto the plasma tail and a plasmoid propagating away from the nucleus. (d) Phases I and II in the *x*-*z* plane correspond to the thinning and disconnected tail.

$y = z = 0$ km), plasma density is high because of the dynamic compression of solar wind ram pressure.

[36] In the right panel of Figure 3a, tail rays can be seen forming and folding toward the tail around $T = 17{:}30$ h. Usually such frontside magnetic reconnections accelerate two bulks of plasma flow shooting along the field lines or tail rays as a sling shot effect. In our result compared to the left panel of Figure 3a, a counterintuitive process can be found. The bulk of the plasma is not only moved along the field lines as elongating tail rays, but also compressed together with the frozen-in magnetic field and folded toward the tail current sheet. Such a colligated movement is the combined effect of frontside reconnection and the hydrodynamic effect of ambient plasma flow.

[37] Figure 3b corresponds to phase II of the disconnection event. In the left panel around $T = 20$ h, the tail becomes thinner than in Figure 3a, while the tail rays continue to fold toward the x axis. The tail ray appearance in both panels of Figure 3b is a candidate for ''broken'' tail rays which are observed occasionally during some DEs. This is also consistent with the images in which the tail rays can be either far or close to the tail [*Brandt et al.*, 1999]. In the same plot, plasma can be seen being compressed into the tail current sheet to increase the tail density in that region. As a consequence, magnetic reconnection starts in the tail current sheet.

[38] In the right panel of Figure 3b, the tail rays overlap with each other as they continue to move antisunward after $T = 21$ h. Although the majority of the HCS has already passed the contact surface region, the decrease in plasma density and momentum makes the contact surface even smaller. The magnetic field starts to reconnect around $x = -8000$ km in the tail current sheet. There is no sunward bulk flow in the tail in this stage, indicating the magnetic reconnection breaks the tail current sheet into a Y plane instead of an X neutral plane [*Galeev et al.*, 1978]. This result can be understood if we realize that the solar wind dynamic pressure provides the driving force for this tail magnetic reconnection.

[39] Shown in Figure 3c are phases III and IV of this disconnection event. After $T = 22.5$ h, as the plasmoid recedes farther into the tail, the magnetic field becomes less compressed as the plasma accelerates to catch up with the supersonic solar wind speed. The field lines reconnected in the current sheet are propagating faster than the plasmoid, so there is no longer any significant magnetic reconnection in this phase. In the left panel the Y plane of the tail reconnection evolves into an X plane and propagates to ($x = -1.2 \times 10^5$, $y = z = 0$ km). Two plasmoids can be found on both sides of the X plane. The plasma on the left is compressed by both the solar wind flow and the counterstreaming magnetic tension force. Consequently, the plasmoid on the left side has a much larger density than the plasmoid on the right. Half an hour later, the left plasmoid passes the distance of 1.2×10^5 km, as shown in the right panel.

[40] In Figure 3c, the configuration of magnetic filed lines is gradually evolving to a stage consistent with the resistive MHD results of [*Konz et al.*, 2004], in which tail magnetic reconnection during such DEs is examined. Compared with the two-dimensional Konz et al. result, which focuses more on the microphysical details, our ideal MHD model is using a reconnection process created by numerical diffusion to study the overall dynamic process. Similar cases have already been studied [*Fedder et al.*, 1984; *Schmidt-Voigt*, 1989; *Wegmann*, 2000], where no tail rays were found and a similar density enhancement propagating along the tail was found but not recognized as a DE. Here using our model with the contact surface and tail rays resolved, as well as the ability of handling sharper density gradient we believe this left plasmoid better represents the start of a DE.

[41] In the right panel of Figure 3c, the separation of plasmoid and HCS (represented by the location of the X plane) suggests that once the plasmoid is combined with and accelerated by the tail reconnection, the recession speed of this disconnected tail is controlled directly by the mass-loaded solar wind bulk flow, not by the magnetic reconnection in the tail. Gradually, the newly born ions fill into the contact-surface region to balance the solar wind compression, forming a new ion coma while extending into a new ion tail. This process is referred to as phase IV.

[42] To study the DE phases I and II in the perpendicular plane, the density contour in the meridional plane is shown in Figure 3d. Because most of the plasma moved from the dayside stays out of the x-z plane, observing in this plane, the time variation of the DE is less obvious in the entire process than those of Figures 3a–3c. The two most remarkable stages are shown in the left and right panel of Figure 3d, respectively. In the left panel ($T = 17{:}30$ h), we can see the foot point of frontside disconnection at ($x = 5 \times 10^3$, $y = z = 0$ km) and the thinning of the tail, while in the right panel ($T = 22{:}30$ h) we can see the foot point of tail disconnection behind ($x = -5 \times 10^4$, $y = z = 0$ km). It should be mentioned that in the right panel of Figure 3d, there is a density peak around ($x = -5 \times 10^4$, $y = z = 0$ km), which is coincident with the peak in the left panel of Figure 3c, marking the cusp of a density cone. This cone is hollow inside, while its wall appears broader in the y direction than in the z direction. This cusp is the closest location to the nucleus where the disconnected tail starts to shoot antisunward. The compressed plasma between the cusp and the Y plane has been referred to as the left plasmoid in our illustration to phase III. A three-dimensional plot with similar shape can be seen in the work of *Yi et al.* [1996].

[43] Shown in Figure 4 are the ion column density contours around the contact surface for different phases of the DE. The column density is integrated along the z direction. The unit in the plots is 6×10^{10} amu/cm^2, which is the same in all column density contour plots in this paper. Such line-of-sight column densities are the assembly of all ions instead of a single ion species; they should not be directly compared quantitatively to observational images of either CO^+ or H_2O^+ ion tail [i.e., *Haberli et al.*, 1997]. However, such column densities do serve to indicate the morphological images that would be observed in either CO^+ or H_2O^+ images of a TD-driven DE.

[44] In Figure 4a from about 16 to 18:30 h, tail rays and tail thinning can be observed as illustrated in the two-dimensional slices. These two images are morphologically close to the column density contour with a 20-min exposure in Figure 4c, which is cut from 6 May, 2:05 UT in Figure 9 in the paper by *Bonev and Jockers* [1994], with permission from ''Elsevier''. It should be noted that in the case presented by *Bonev and Jockers* [1994], there is no discon-

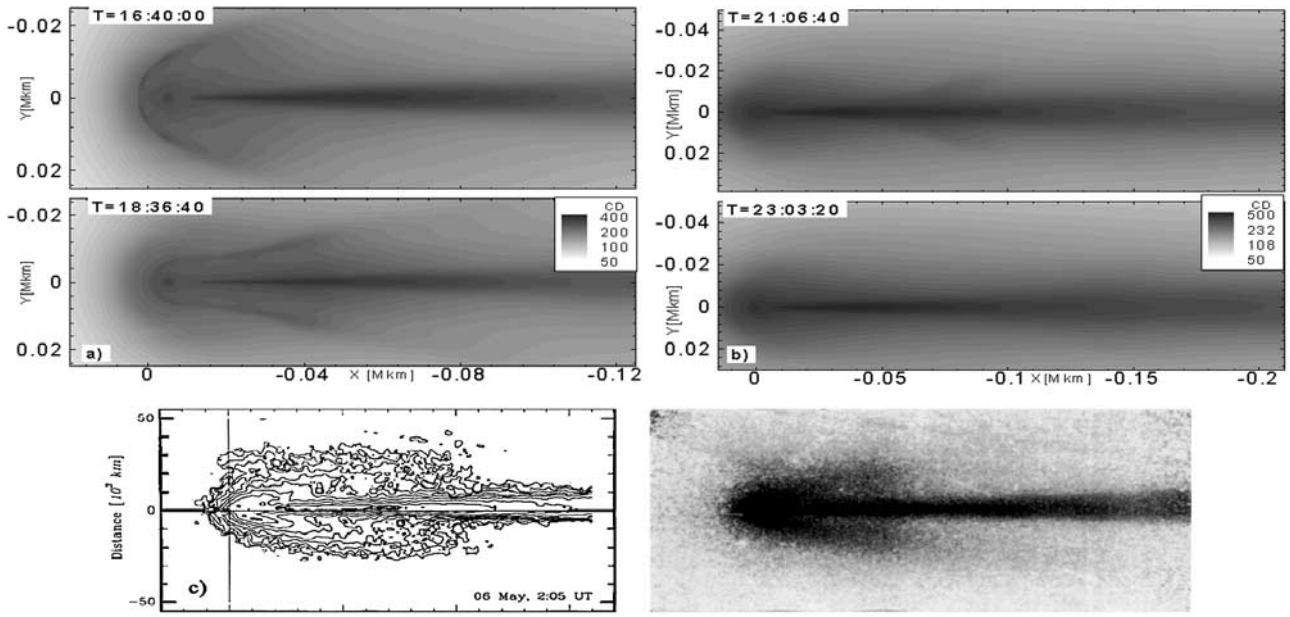

Figure 4. Images looking along the Z direction: column densities (CDs) showing tail rays with no observable disconnection. The CD unit here is 6×10^{10} amu/cm^2. Later figures in this text use the same notation and unit. (a) Phase I. (b) Phases II–IV, tail rays folded into the tail, but no disconnections can be observed. (c) Column density of water ions in comet Austin, 6 May 1990: the distances are 10^4 km. Figure from *Bonev and Jockers* [1994].

nection of the tail following the tail rays. The whole evolution process will be studied in our case 2 in next section. Later on, in the upper panel of Figure 4b at 21 h, we can see the folding of the tail rays into the plasma tail. However, once the tail rays have merged into the plasma tail along the x axis, no disconnection can be recognized due to the thickness of the tail current sheet, as can be seen around $T = 23$ h.

[45] Shown in Figures 5a and 5b are the ion column densities integrated along the Y direction. In this direction

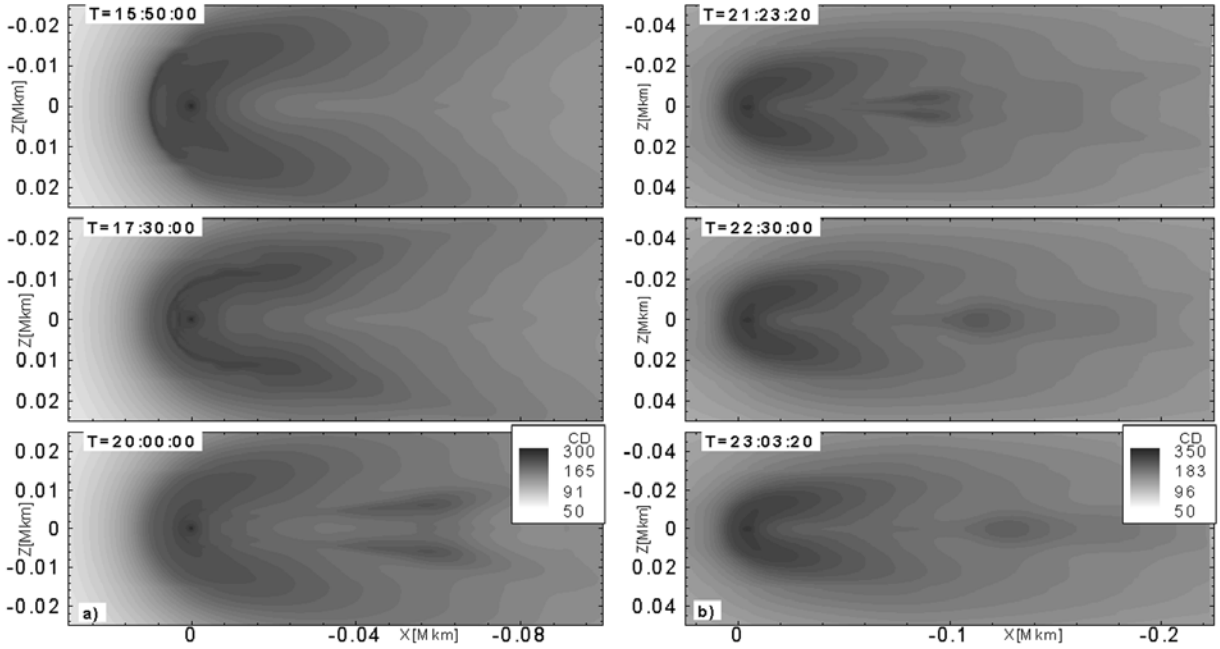

Figure 5. Images looking along the Y direction: column densities showing tail rays followed by tail disconnection. (a) Dayside plasma compressing and moving toward nightside and folding toward the ecliptic plane resembling tail rays. (b) Tail rays folded into a plasmoid and drifting away. The column density in the plasmoid is significantly higher and thicker than locations closer to the nucleus, appearing as the head of a disconnected tail.

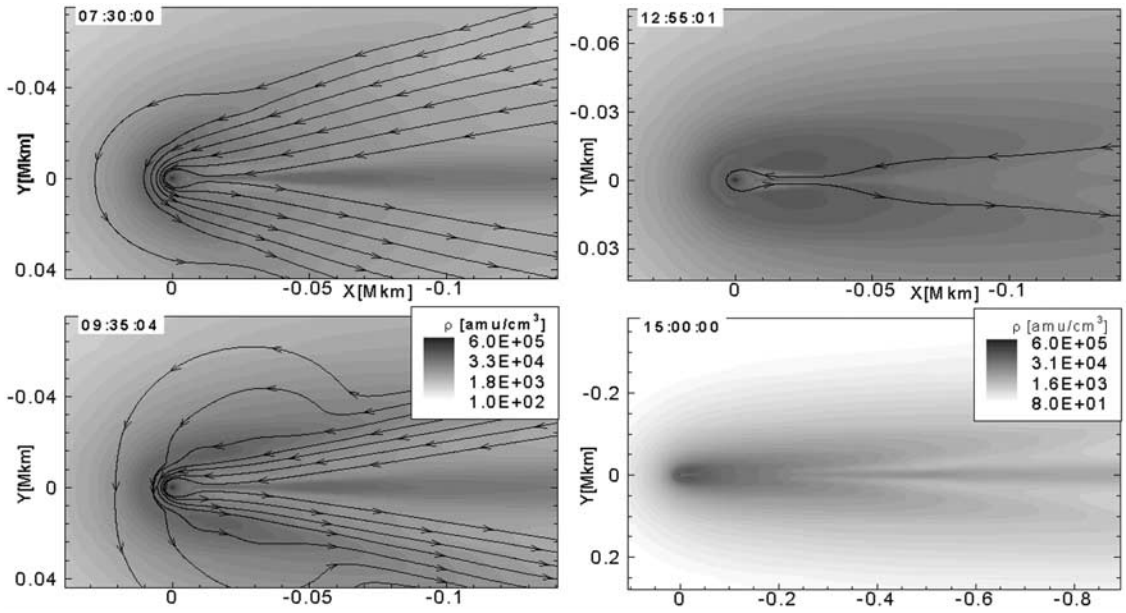

Figure 6. Case 2, effect of a 90° TD; time variation of density contours in *x*-*y* plane. The spacial scale in the last panel is larger than in the rest three panels.

the tail is much broader compared with those of Figure 4, but the four phases of the DE are obvious. In the middle panel of Figure 5a at 17.5 h, we can see the two tail rays. In addition, the width of the tail in this middle panel is around 4×10^4 km, which is thinner than the tail width in the upper panel and that of Figure 2d, which measures around 7×10^4 km.

[46] After $T = 20$ h, in both the lower panel of Figure 5a and the upper panel of Figure 5b, the tail rays are stretched further and compressed into the tail. This local rise in local column density can already be recognized as the start of the disconnected tail. In the middle panel of Figure 5b around 22:30 h, the head of the disconnected tail has merged into one bulk plasmoid (around the "O" point), which can be found around ($x = -1 \times 10^5$, $y = z = 0$ km). This location is twice as far as the position of the cusp plotted in Figures 3c and 3d at the same time because the most observable part of the plasmoid is the density peak marked in this column density plot instead of the sharp density cusp.

[47] Phase IV can be observed in the lowest panel of Figure 5b after 23 h, where the density around the contact surface starts to recover into the same shape as the initial steady state. Around $0 > x > -1 \times 10^5$ km, part of the regenerated new tail is formed and stretching out while the start of the old tail at ($x = -1.3 \times 10^5$, $y = z = 0$ km) continues to propagate antisunward along the tail. Compared to the same time slot in Figure 3c, the location of this disconnected head lies right behind the *Y* plane. It is interesting to find that the brightest spot of this disconnected tail is always this leading plasmoid, whose width is always smaller than the width of the tail. Despite the fluctuations created in real solar wind conditions, this characteristic agrees with the features found from the images of *Snow et al.* [2004].

[48] Combining the plots in Figures 4 and 5, one can construct the idea of a hypothetical image sequence observed from an arbitrary angle which is comparable with DE pictures recorded. Such analysis has been initiated by *Yi et al.* [1996] for DE studies. Our study shows that for observation angles of 30°, 45°, and 60° relative to the IMF plane, the column density contours appear to be more like the parallel view in Figure 5 rather than the perpendicular view of Figure 4. Considering the violent nature of solar wind, the chance for a comet-IMF interaction region to be exactly perpendicular to the ground-based observers throughout such a 2 days interval is quite small. This characteristic implies that DEs will be observable to ground-based observers most of the time, except when the angle between the IMF and the line-of-sight is close to 90°. Moreover, in reality the leading edges of the disconnected tail are quite sharp so it can be seen even close to 90°. Such results require more violent interactions or more mass accumulated into the tail.

3.2. Case 2, Interaction With a 90° TD

[49] In reality, the HCS can take a range of varied forms of TD. Based on case 1, we studied a few typical TDs different from the $\mathbf{B}_y$ reversal.

[50] The second case we studied is a 90° rotation from $\mathbf{B}_y$ to $\mathbf{B}_z$. Across a tangential discontinuity, without any jumps in other parameters including $|\mathbf{B}|$, the magnetic field can be rotated by any angle. In this case, $\mathbf{B}_1 = (0, B_\infty, 0)$ is jumped to $\mathbf{B}_2 = (0, 0, B_\infty)$. A physical explanation for a 90° TD is a sudden decrease in $\mathbf{B}_y$ with a sudden increase in $\mathbf{B}_z$. This will result in a change in the distribution of the induced magnetic field.

[51] Shown in Figure 6 are the density contours in the initial IMF plane (*x*-*y* plane) at different stages of case 2. At 07:30 h, in the upper left panel, when the TD encounters the frontside contact surface boundary, the decrease in the B_y component can be observed. The start time of these plots is earlier than that used in previous section because a closer upwind boundary is used to speedup the simulation process. Our discussions later will show that there is no difference created by such a boundary change. Two hours later, at

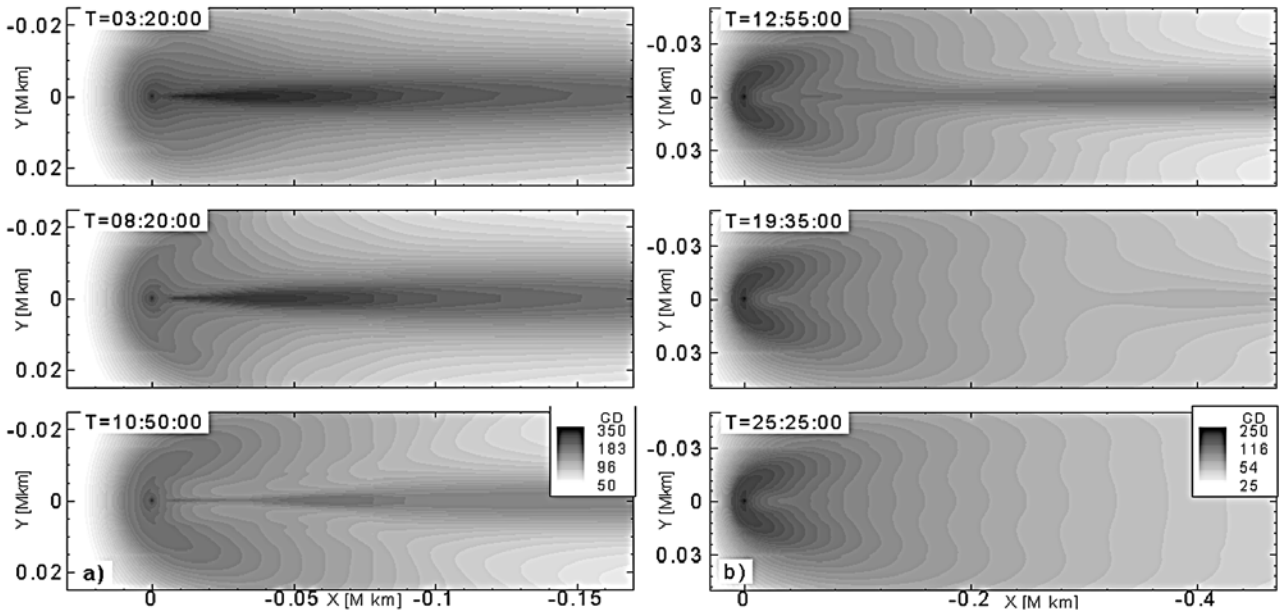

Figure 7. Case 2, column density contour in *x*-*y* plane. The spatial scale in the right panel is twice the scale in the left panel.

09:35 h, the lower left panel shows that the tail rays start to form. The three outer most field lines in the lower left panel show the *x*-*y* projection of the field lines in the region where the $\mathbf{B}_y$ component gives way to the $\mathbf{B}_z$ component. Comparing the two plots in the left panel of Figure 6, we can see that the total density of the plasma in this region increased with time, while in case 1 the change in total density is not so obvious. This increase indicates that plasma is moved from corresponding regions in the *x*-*z* plane to fill in this region to form tail rays, instead of being compressed into tail rays.

[52] In the upper right panel in Figure 6, the tail rays become thicker and larger, by evolving into the two wings of the steady state view in Figure 2c, while the old tail becomes shorter and fainter. At 15:00 h in the lower right panel, a larger region is shown. It can be seen that the tail becomes thicker in front of -0.2×10^6 km, while the thin old tail farther than this location is still observable and not changing. We can thus estimate that the tip of the bent TD has propagated to -0.2×10^6 km along the *x* axis.

[53] Figure 7 gives the time evolution in column density in this *x*-*y* plane. It appears that during this process, the thin tail becomes thinner and fainter while the frontside plasma lengthens into tail rays. Between 8:20 and 10:50 h in the two lower left panels, thick tail rays appear and become fainter while no enhancement close to either side of the tail can be seen. Subsequently, a thicker tail emerges in a larger scale, while the old thin tail dissolves away. From the left panels, we can see that the evolving speed of the TD-comet interaction in the frontside of the comet occurs on the same timescale as in case 1. This similarity between pressure driven evolution and magnetic-reconnection driven evolution indicates that the frontside magnetic reconnection in case 1, although eruptive in compressing the plasma density and heating the ambient particles, is not speeding up the whole flow field. The plots in Figure 7 are consistent with plots made by *Rauer et al.* [1995, Figures 17 and 18].

[54] Shown in Figure 8 are the density contours in the *x*-*z* plane. The total density is decreasing with time in this plane, while the tail evolves from a thick short tail into a thin long tail. In the middle of this transition, two thin tail rays can be observed. The field lines in both plots of Figure 8 mark the approximate position of the TD. From the lower panel we can see that an increase in the $\mathbf{B}_z$ component does have a compressive effect on the plasma tail, by driving part of the plasma into the two-tail rays.

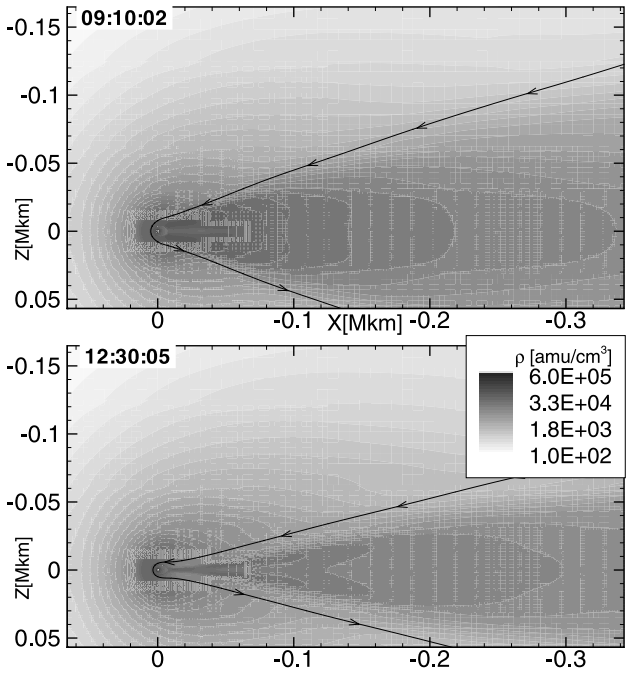

Figure 8. Case 2, time variation of density in *x*-*z* plane.

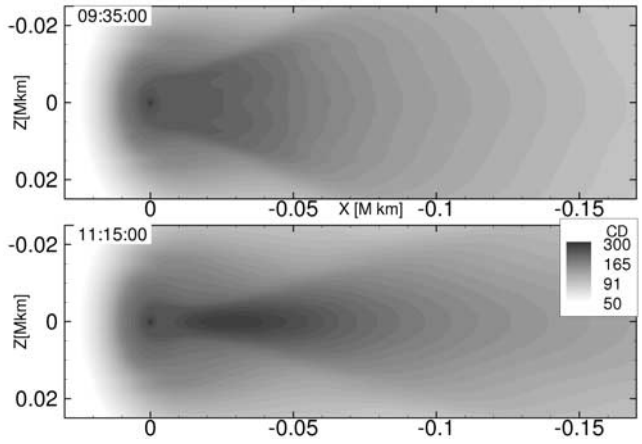

Figure 9. Case 2, time-evolution of column density contours in *x*-*z* plane.

[55] Figure 9 shows the change in column density in the *x*-*z* plane of this process. Tail rays can be seen at 9:35 h in the upper panel while the disconnection is not observable in the tail. It is interesting to find that such tail rays appear both in the *x*-*y* plane and the *x*-*z* plane during the time era between 9:35 and 10:50 h. Subsequently, a thin tail is formed by the compression of the B_z component.

[56] As a summary, the effect of a 90° TD has the following differences from a 180° TD: The tail rays in case 2 not only last longer than case 1, they also appear thicker than case 1 at all stages. No obvious disconnection in the tail can be observed, which is consistent with the work of *Rauer et al.* [1995] and also *Wegmann et al.* [1996] which simulated a different comet.

[57] To determine the reason behind the differences between the two cases, we investigated the evolution of pressure distribution around the contact surface in case 2. Figure 10 compares the time variation of magnetic pressure and total pressure on a line cut from (0, 1.2, 0) to (−15, 1.2, 0) × 10^4 km. The dash-dotted line is magnetic pressure taken at 09:00 h, when the TD has just reached the frontside of the

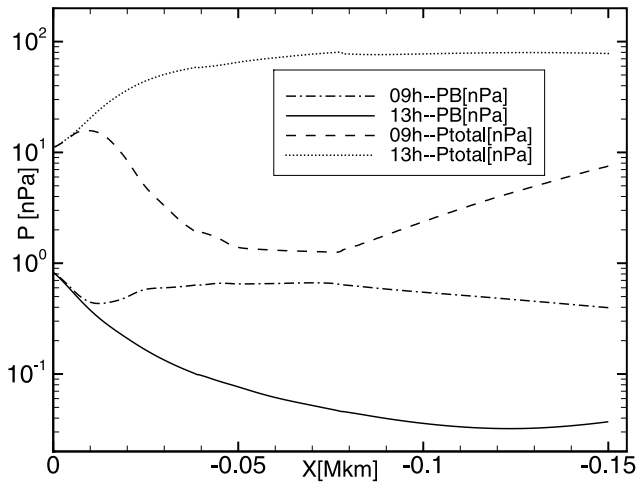

Figure 10. Pressure distribution along the $y = 1.2 \times 10^4$ km line in the *x*-*y* plane during the encounter of the 90° TD.

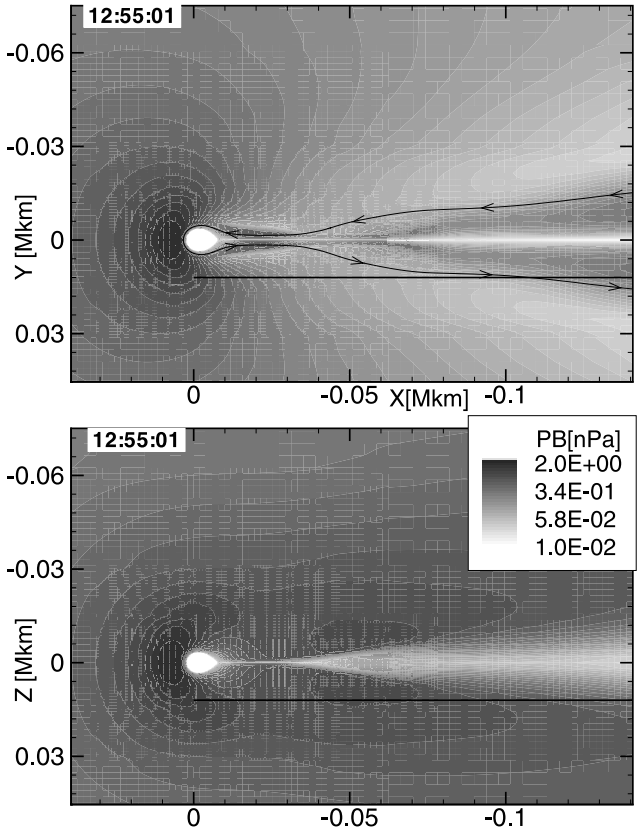

Figure 11. Case 2, magnetic pressure distribution in two planes (*x*-*y* and *x*-*z* plane) at 13:00 h.

contact surface, causing two thin and wide open tail rays, while the solid line is magnetic pressure taken at 13:00 h, when two thick tail rays have appeared in the *x*-*y* cut of Figure 6. In the tsaveregion farther than -4×10^4 km, the local magnetic pressure decreases and the plasma tends to fill into this region. As a consequence, a large ram pressure is sustained by the mass-loaded solar wind, which can be seen from the dashed line and the dotted line in Figure 10. It is this decrease in magnetic pressure that allowed the plasma to migrate into both sides of the tail to form tail rays. The origin of such plasma can be traced in Figure 8, where a large amount of plasma forming the thick tail in the *x*-*z* plane is removed after 13:00 h. More detailed simulations are needed to show how the plasma is peeled off and moved into the *x*-*y* plane.

[58] Comparison of the two magnetic pressure contours in Figure 11 shows where this plasma originates. The upper panel shows the magnetic pressure contours in the *x*-*y* plane. The position of the line cut taken in Figure 10 is marked by the straight black line. In the lower panel, the *x*-*z* plane is shown. The black line drawn here marks a line cut from (0, 0, 1.2) to (−15, 0, 1.2) × 10^4 km. The piled up magnetic field around a comet is pure induced field. Thus for a steady state problem, rotating the IMF field direction from *y* to *z* essentially means an exchange in the coordinate system by switching the *y* and *z* axis. As for this time-variable case, the condition of *x*-*z* plane in the lower panel at 12:55 h reveals the condition of *x*-*y* plane at an earlier time. We can see that comparing the magnetic pressure P_B at the locations the lines marked, the value in the *x*-*z* plane is much larger than in the *x*-*y* plane. This difference effectively shows a

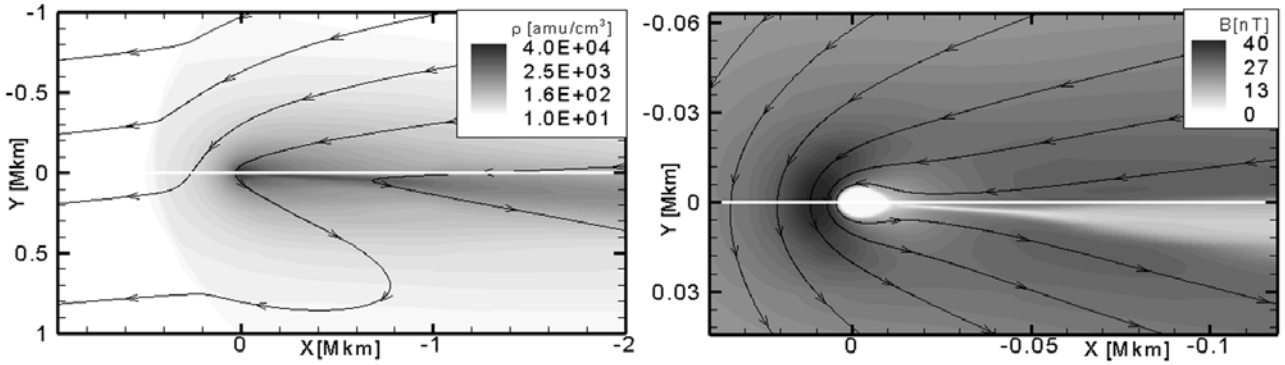

Figure 12. Case 3, a steady state approach with large B_x component, for nonzero B_y conditions. Left: density contour around the bow shock with magnetic field lines. Right: magnetic field contour and field lines around the contact surface. Both show a rotated tail. White line marks the Sun-Comet line.

decrease of P_B over time, which is consistent with the change from 09 to 13 h in Figure 10. On the other hand, the condition along the second line cut from (0, 0, 1.2) to (−15, 0, 1.2) × 10^4 km changes in the completely reversed direction. Comparing these two trends, namely decreasing along the line in the *x*-*y* plane, against the increasing along the line in the *x*-*z* plane, we can conclude that the magnetic pressure has driven plasma from the marked location in the *x*-*z* plane into the marked location in the *x*-*y* plane over the period of time shown. In addition, different from case 1, there is no obvious condition to trigger substantial magnetic reconnections in case 2, and thus there is no obvious magnetic reconnection process found in the tail. Thus these tail rays can only move by diffusion due to the P_B gradient described above instead of folding into a plasmoid and traveling away as the head of the disconnected tail.

[59] Combining this with the density change in these two planes, we can conclude that the process of a 90° TD encounter with a comet plasma is a steady dynamic movement of plasma from the *x*-*z* plane into the *x*-*y* plane (the IMF plane) with the field lines. In addition to this, as stated in Figure 8, a small portion of plasma population is compressed by the B_z component into the newer tail and propagated away. It can be seen that the magnetic pressure change by itself will not produce a DE, more eruptive procedures like magnetic reconnection in case 1 are needed to sustain an observable broken tail.

[60] In a more generalized way, whenever the angle of field rotation in the interacting TD is larger than 90°, there is a negative B_y component after the TD, compared with the B_y before the TD. Such a negative component will result in DE appearances similar as those caused by 180° TD in case 1. A simulation not presented here with 120°-field rotation in HCS confirmed this conclusion with behavior that closely resembles case 1 result. This result disagrees with the estimation of "50% effect" on p 769 by *Wegmann* [2000], and may simply because of our improved resolution.

3.3. Case 3, The Effect of the B_x Component

[61] In real solar wind data the HCS is not always perpendicular to its propagation direction against the comet, so a B_x component is present in such interactions. To study such a B_x component, our case 3 investigates the effect of a large B_x with nonzero B_y on a steady state comet. We choose a B_x five times larger than the average IMF magnitude to make the result easier to distinguish. Figure 12 shows the effect in two different scales for steady state MHD model runs with B = (20, 1.96, 0) nT. The white solid line marks the position of the *x* axis. The effect of B_x to the tail is observable at a comet-centric distance of 10^5 km. At this distance the tail is rotated about 4° to the +*y* direction. We can see that the subsolar distance of the bow shock is not affected by the B_x component, while the entire density distribution behind the bow shock is rotated to the −*y* direction by about 5°. The angle between IMF and the tail is about 11°, while for our first two cases this angle is 90°. This result indicates that the B_x component does not have a large effect on the density distribution of cometary plasma when B_y is not negligible. For a tilted TD with a jump from B_1 = (B_∞, B_∞, 0) to B_2 = ($-B_\infty$, $-B_\infty$, 0), the time evolution (although not shown here) is similar to case 1, while the broken tail propagates along the track of the old tail, instead of moving sideways. This result suggests that magnetic discontinuity by itself cannot result in the displacement of the broken tail. There should be other reasons, such as orbital movement of the comet or turbulence accompanying the HCS, for the broken tail to shift sideways as observed and discussed by *Niedner and Brandt* [1978, Figure 9].

3.4. Case 4, Recurrence Interval of Multiple TDs to Trigger a DE

[62] *Yi et al.* [1993] have shown a spectacular example of a sequence of DEs in the tail of comet Halley in April 1986. In our study, multiple pairs of tail rays can be observed as multiple TDs interacting with a comet during certain time intervals. The typical effect of multiple TDs can be summarized in our case 4, in which a comet interacting with two TDs with B_y field reversals are studied. The interval between the two TDs is 2 h. Plotted in Figure 13 is the time variation of the column density. The upper left panel shows the two compressed density sheets in the frontside at 09:30 h, with the first sheet extending to the nightside. The lower left panel shows the shapes of two pairs of tail rays at 11:40 h, with the leading pair broken from the nucleus. On a larger scale, the upper right panel shows the extended tail rays with the relaxed shorter tail at 13:20 h. The lower right panel shows the broken tail down stream and the elongated new tail at 23:00 h. This finding is consistent with the descriptions of folding tail rays occurring with a disconnected tail by *Niedner and Brandt* [1978].

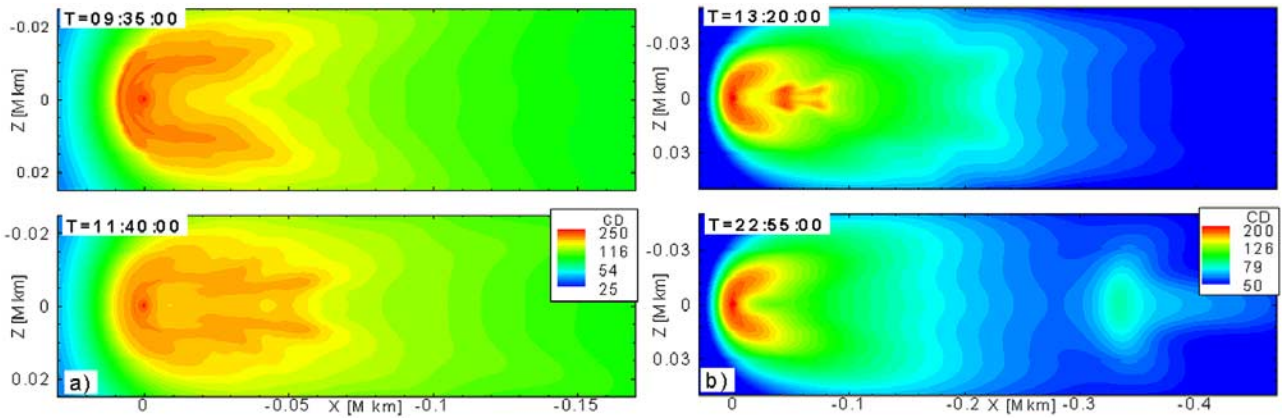

Figure 13. Case 4, two TDs with a 2-h interval. Column density contours (logarithmic levels) observed from above the IMF plane.

[63] From Figure 13 we can see that multiple TDs in the solar wind can create multiple frontside disconnections, resulting in multiple sharp tail rays, but when those tail rays fold into the tail, the tail rays caused by the later TD will catch up with the first one to form a single tail disconnection. This catch-up also supports the suggestion that the reconnection in the tail does compress and accelerate the bulk plasma in the tail, while outside the reconnection region, the acceleration is only driven by the ambient solar wind flow. Also, from the lower right panel we can see the shape of disconnected tail appear not only stronger than the ones created by single TDs presented in our case 1, but also closer to observational images than the result of case 1. At its perihelion, a comet usually crosses the flaring HCS several times. This means that reality is more like case 4 than case 1.

[64] On the other hand, if these crossings take place with intervals less than 2 h, only one DE will be observed. Our simulation case with 1-h interval between two TDs shows merged tail rays, implying shorter intervals are equivalent to a single TD. This also suggests that the typical timescale for energy to be restored, or for a frontside magnetic barrier of such a comet to recover is about 2 h. In another simulation of this type (not shown here) with a 4-h interval between the two TDs, we observed two consecutive DEs moving along the tail until they diffused away. It should be noted that although the time periods of 1, 2, and 4 h are intrinsic features of the cometary plasma environment, they are dependent on both solar wind condition and cometary production rate. Different comets, under different solar wind conditions, as well as the relative speed the HCS moves against the comet, may provide different timings. Such findings can be used to explain the fact that appearance of tail rays is much more frequent than the appearance of DEs. These features above also suggest statistical studies to be made comparing number of DEs with the number of comet HCS crossings.

4. Discussion

[65] In section 3, magnetic reconnections are discussed to be essential for DEs to be triggered by an HCS. However, the model we are using is an ideal MHD model which is not strictly speaking suitable for magnetic reconnection study itself. On the basis of the successful reproduction of observational images and time-dependant processes with our high resolution calculations, as well as previous publications in which HCS related magnetic reconnections in both front and tail plasma are studied, we do believe that reconnection process is the trigger of such HCS-related DEs. Although not proportional to the physical resistivity, the numerical resistivity introduced into our result by truncation errors is found to be fairly low; that is, in the pile up region in front of the contact surface (x = 5000 km), we found the numerical resistivity is effectively on the order of 10^3 Ωm. This value is five orders of magnitude larger than classical resistivity estimated from binary collisions [*Spitzer*, 1956]. Nevertheless, the limitations of ideal MHD may stop us from calculating the reconnection rate and thus give a better reproduction of the start time of the DE as well as a more accurate prediction of the time period between HCS encounter and tail ray formation.

4.1. Recession Speed

[66] The recession speed of a DE can be measured from images taken at different times. Measured from the images provided in the work of *Brandt et al.* [1999], the recession speed is quite different for various DEs. Typically, for a specific DE, the recession speed increases as a function of time as the DE travels down the tail.

[67] In our numerical tests we found that the recession speed varies with most of the key parameters in the interaction region, such as the cometary production rate, and the speed, density, and magnetic field in solar wind. In addition, multiple discontinuities can speed up the recession speed. In this way tracking the affecting factors of this recession speed in the future may provide information of the ambient solar wind. The study of how the recession speed responds to these conditions is beyond the topic of this paper.

[68] Figure 14 gives the recession speed measured from our case 1 compared with those from published DE images. The solid line is the speed of the receding tail from case 1, varying with time. The foursquare data points with error bars are the recession speed measured from DE images by *Brandt et al.* [1999]. It can be seen that the acceleration slows down after the speed reaches 40 km/s during the transfer. Although it is too small a sample for statistics, the simulation agrees well with the data points we have. In the previously published paper of *Yi et al.* [1996], the recession speed can be measured from their model plots. Unfortunately, their recession speed is

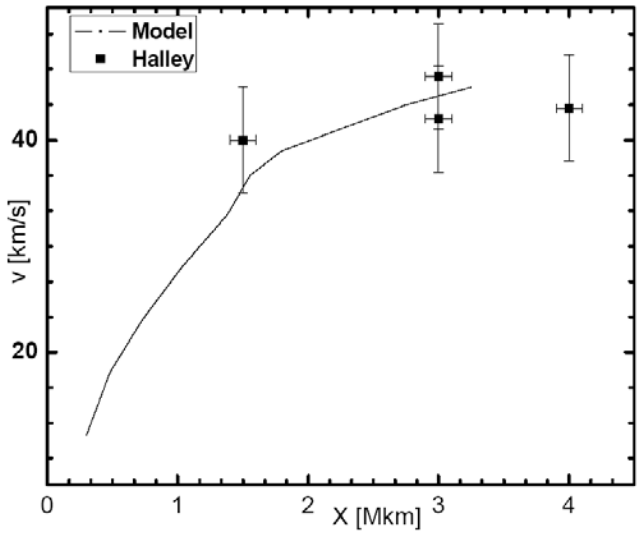

Figure 14. Recession speed compared with the values measured from Halley pictures of *Brandt et al.* [1999].

almost an order of magnitude larger than the observational measurement. It can be seen that for the first time, our cometary plasma simulation with a well-resolved contact surface does give a more realistic quantitative description of the HCS-related tail disconnection process. This region is important not only because the magnetic field increases by 50 times around the standoff point when solar wind flow meets the cometary flow and both flow speeds become zero, but also because for such Halley type comets, 30% [see Appendix B, equation (B1)] of the picked up ions are loaded within comet centric distance of 1×10^4 km. Our simulation test using a lower resolution not shown here in fact gives a less accurate description of the DE as well as a faster recession speed than observations.

[69] Figure 15 shows the comparison between our standard model result and a comet Hyakutake measurement. The thick dashed line is our standard model based on Halley conditions. The thin black dash dotted line and the plus symbols are the best fit for 1996 Hyakutake measurement from Figure 4 of *Snow et al.* [2004], with permission from Elsevier. Both data and simulation show the same speeding up pattern in the recession process. Our numerical tests show that with different production rate and solar wind conditions, the slope of this curve can vary broadly. No particular attempt was made to tune the parameters to obtain a more exact fit, because of the reasonable enough match. Further investigations with better resolution in real-time tracking of the receding breakpoint should be able to provide better statistical laws of the relationship between recession speed and production rate, as well as solar wind conditions. *Niedner* [1981] and *Voelzke and Matsuura* [1998] give a good collection of recession speed measurements to facilitate such simulations. On the other hand, the propagation of the incident discontinuity interface can take any speed. Here we are limited by using the same speed as the solar wind speed, while further recession speed study should be based on a range of propagating TDs.

4.2. Conclusions

[70] The four cases illustrated above can be used as demonstration to support the empirical theory relating

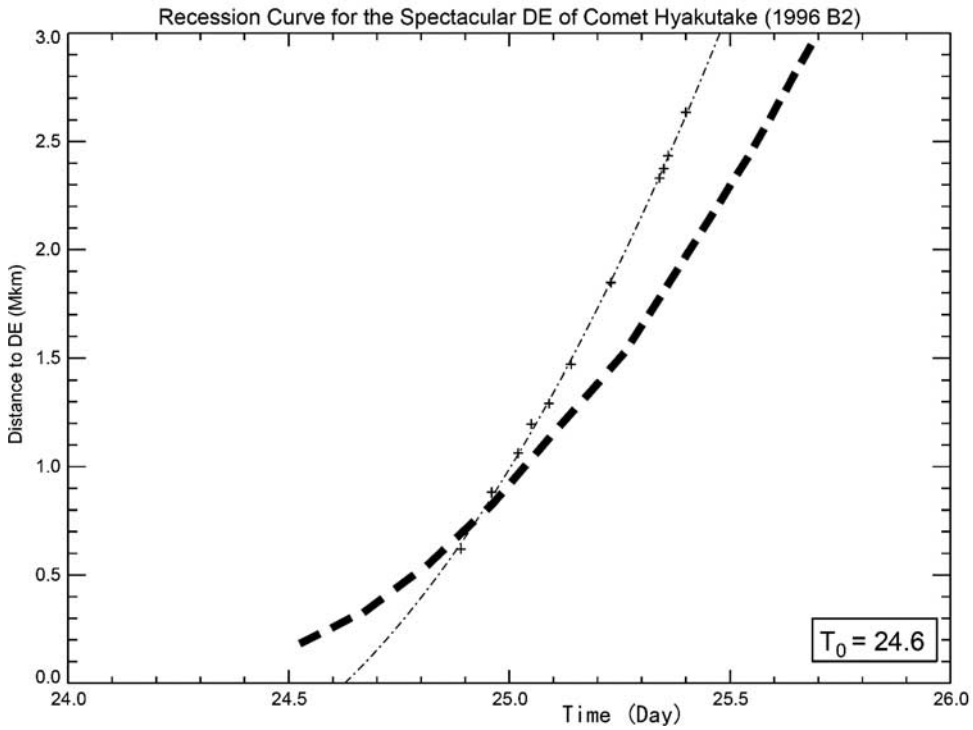

Figure 15. Recession speed compared with Hyakutake images. The plot is extracted from *Snow et al.* [2004], with permission from Elsevier. The thick black dashed line is our model result superimposed on Snow's plot using the same scale.

HCS with DEs proposed by *Niedner and Brandt* [1978]. Our MHD model can reproduce disconnection events by simulating a heliospheric current sheet represented by a tangential discontinuity passing through the comet plasma. Our simulation results show that if such DEs happen at the time the comet tail can be seen, most of such DEs should be observable. Solar wind TDs need to have a field rotation of larger than 90° to trigger the condition for magnetic reconnection to happen both in the frontside and the tail and therefore to cause a DE. The reproduction of the plots by *Rauer et al.* [1995] explains why they were not able to trigger a DE with a TD: a rotation angle larger than 90° needs to be used. For instances where multiple HCS crossings happen, the interval of two adjacent crossings should be larger than 2 h. Also, such DEs caused by multiple crossings appear closer to real images in two ways: more tail rays can be seen and the disconnected tail appears stronger with a shape that better resembles the observed images. Our case 4 also suggests that the typical restoration timescale of the frontside magnetic barrier in a Halley sized comet is about 2 h. The dynamic similarity of our model to the observations is furthermore reflected in the recession speed investigations. Compared with the preceding simulations, our multiscale model results which can resolve the major ion-neutral reaction region is able to reproduce the dynamic processes including the tail recession speed. Our time evolution of the DE is comparable to the observations too, which disagrees with the claim by *Wegmann* [2000]. However, the study of the B_x component effect shows the possibility of other possible causative factors for DEs with shifted tails, such as interplanetary shocks as suggested and studied by *Wegmann* [2000].

[71] There are yet a number of questions not answered, such as, are HCS crossings the only types of processes that trigger cometary disconnection events? In known solar wind conditions, how well does the simulated column density compare with ground-based CO^+ or H_2O^+ images? Future work will be focused on the cometary response of a broader series of time-variable solar wind discontinuities, i.e., interplanetary shocks and magnetic clouds, and a series of chemical-reaction based multispecies studies. Our understanding of the dynamic feature of recession speed is only a beginning. More details should be investigated to find out the relationship between the speed and the solar wind conditions. Such a parameter study can serve as a valuable laboratory for MHD theory.

Appendix A: Increased Charge Exchange Rate

[72] Different from previous models of the comet ion production rate, we have implemented the reaction between minor cometary neutral species and solar wind protons. When a water molecule decomposes, an oxygen atom and two "cold" hydrogen atoms are created [*Combi and Feldman*, 1993; *Haberli et al.*, 1997]. Usually in the inner coma region the hydrogen density is two magnitudes smaller than the heavy neutral density. Similar to the charge exchange reaction between water species ions and neutrals, the charge exchange reaction $H^+_{hot} + H \rightarrow H + H^+_{cold}$ is important because of the large cross section caused by resonance [*Combi et al.*, 2004]. This reaction will not change the mass loading rate, but the momentum and energy sources are modified. Therefore in our single species approach of cometary MHD, the neutral density used to calculate the mass source should be smaller than the one used to calculate the momentum loss. An exponential density distribution based on the water neutral density is used to estimate the loading rate of these hydrogen atoms. To be consistent with the density distribution of water species atoms, a larger ionization scale length is also estimated. This scale length will cause hydrogen density to decrease more slowly than the decrease of heavy neutral density. Such additional momentum loss slows the flow down more rapidly than those without such a term. The effect should be a larger magnetic cavity with similar ion density inside the cavity. For larger comets like Halley and Hale-Bopp, the effect should be more obvious than for smaller comets [*Combi*, 2000]. How such an extra charge exchange might affect the recession speed is beyond the scope of this paper. Eventually, such modifications will give way to multispecies approaches in our future work.

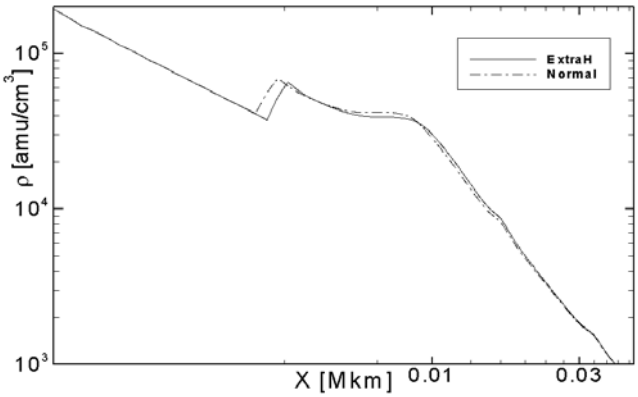

Figure A1. Effect of an extra amount of cometary hydrogen charge exchange: density log-log cut along the x axis near the contact surface for comet Halley. Solid line is the result with enhanced charge exchange rate, while dash-dotted line is the one with normal charge exchange rate.

[73] Plotted in Figure A1 is the log-log density value around the contact surface along the x axis. The plot is the line cut from two steady state runs. For both the two lines, the peak around x = 3000 km marks the location of contact surface. The dash-dotted line is the result with normal charge exchange rate. The solid line is the result with the larger charge exchange rate, which is used for the calculations of the four cases in this paper. The increase in the location of the contact surface is roughly 10%. For locations farther out near or outside the bow shock, there is no obvious difference between these two cases.

Appendix B: Upwind Boundary Location

[74] The ionization and charge exchange process create new ions from the expanding cometary atmosphere. Such newly created cold ions tend to move with the neutrals, which flow differently from the background solar wind. If ionized outside the magnetic cavity, such ions are picked up by the IMF, which is frozen in the bulk solar wind flow. Such a particle-flow coupling process with the change of mass, momentum, and energy involved, is called "mass loading" in MHD. For a Halley type comet, the solar wind

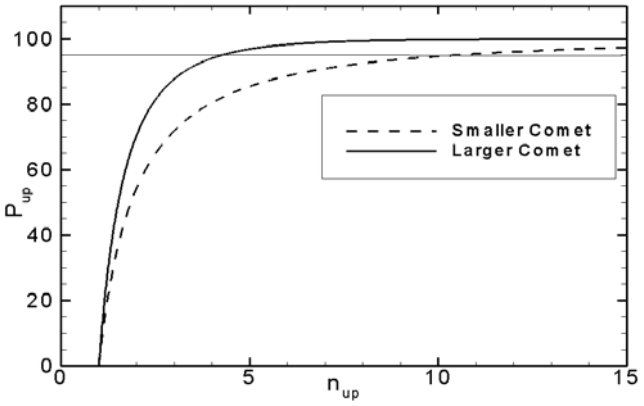

Figure B1. Comparison between a large comet and a small comet with different shock distances: effect of the upwind boundary location on the percentage of mass loading included (P_{up}). The x axis is the ratio n_{up} between upwind boundary and bow-shock distance. The horizontal solid line marks the position of 95% mass loading.

flow speed along the x-axis decreases and drops to zero around 3×10^3 km because of mass loading. Limited by their computational capabilities, previous DE related Halley simulations from other models usually give a smallest grid size of 5×10^3 km. In order to find out the effect of resolution in this region, it is reasonable to calculate the percentage of mass loading in the range between 10×10^3 and 3×10^3 km. The total amount of loaded mass in a certain volume is defined by the volume integral of source term S in equation (5). Such integration shows that the mass loaded within the sphere of cometocentric distance of 10×10^3 km is less than 1% of the total mass loaded around the comet. From equation (5) we can also see this percentage is not dependent on the production rate Q.

[75] However, what matters for the incoming solar wind flow to couple with the picked-up plasma particles and to form the certain structures is the integration along the streamlines. To simplify the problem, we integrate along the streamline coincident with the x axis to get a one-dimensional estimation. Integrations along other frontside streamlines always have longer distances than the streamline we selected but the order of magnitude should be the same. The theoretical integration goes from infinity to the solar wind standoff point at 3×10^3 km. To compare the integrations, this percentage R can be estimated by

$$R = 1 - \frac{\int_{+\infty}^{10\times10^3} \frac{m_c Q f_i e^{-x/\lambda_\infty}}{4\pi\lambda_\infty x^2} dx}{\int_{+\infty}^{3\times10^3} \frac{m_c Q f_i e^{-x/\lambda_\infty}}{4\pi\lambda_\infty x^2} dx} = 1 - \frac{\int_{+\infty}^{10\times10^3} \frac{e^{-x/\lambda_\infty}}{x^2} dx}{\int_{+\infty}^{3\times10^3} \frac{e^{-x/\lambda_\infty}}{x^2} dx} = 29\%, \quad \text{(B1)}$$

where the integral is taken from equation (5) with the integration variable changed to the x coordinate. It can be seen that for comet Halley only 70% of the mass loading responsible for the contact surface formation is accounted for along the streamline outside the second calculation cell at 10×10^3 km with previous resolutions. This deduction verifies the importance of pushing to high resolution around the contact surface.

[76] Furthermore, the calculation of such a flow field integration inspires us to develop a way to determine the upwind solar wind flow boundary for all mass-loaded plasma simulations. For numerical simulations a smaller calculation domain means faster computational speed. To obtain better resolution cometary simulations requires a large number of calculation cells around the nucleus. As *Biermann et al.* [1967] have pointed out, the cometary shock is not a typical planetary bow shock but a mass-loaded weak shock. This makes it a more challenging situation for cometary modelers, because to include most of the mass loading in the calculation domain, the upwind boundary should be much larger than the bow shock distance. All previous simulations including that by *Gombosi et al.* [1997] followed this law by choosing a fixed large number n_{up} (i.e., $n_{up} = 80$) in unit of the shock distance. However, our deduction and estimation show it is not always this critical. Here we try to estimate the effect of mass loading over a certain distance to find out the accuracy of different boundary conditions. The amount of mass loading in the region in front of the shock can be studied as follows.

[77] By changing the R into the ratio P_{up}, which represents the ratio of mass loading in front of the bow shock included in the calculation domain against the total theoretical mass loading in front of the bow shock, we get equation (B2):

$$P_{up} = 1 - \frac{\int_{+\infty}^{n_{up}D_{shock}} \frac{m_c Q f_i e^{-x/\lambda_\infty}}{4\pi\lambda_\infty x^2} dx}{\int_{+\infty}^{D_{shock}} \frac{m_c Q f_i e^{-x/\lambda_\infty}}{4\pi\lambda_\infty x^2} dx} = 1 - \frac{\int_{+\infty}^{n_{up}D_{shock}/\lambda_\infty} \frac{e^{-y}}{y^2} dy}{\int_{+\infty}^{D_{shock}/\lambda_\infty} \frac{e^{-y}}{y^2} dy}, \quad \text{(B2)}$$

where D_{shock} is the subsolar distance of the shock, n_{up} is the upwind boundary location in unit of D_{shock}. In the simplified form of equation (B2), we can see that the integral is not explicitly dependent of the cometary production rate Q, but explicitly dependent on the shock distance D_{shock} and the scale length constant λ_∞. In our argument the P_{up} is relevant to Q only because D_{shock} is always sensitive to Q. A numerical solution can be given to determine the n_{up} as a function of D_{shock}/λ_∞ for a fixed P_{up}. However, for the

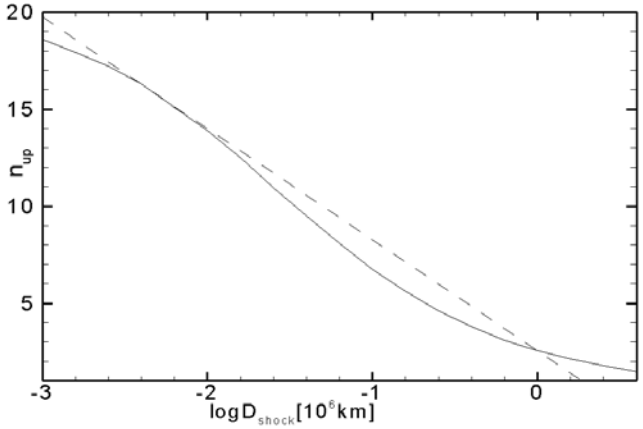

Figure B2. Relationship between minimum upwind boundary position and bow-shock distance.

Table B1. Upwind Boundary Location Requirements for Some Typical Cometary Parameters[a]

Comet Name	Ion Production Rate Q (s^{-1})	Shock Distance D'_{shock} (10^6 km)	Upwind Boundary n_{up} in Terms of D'_{shock} for P_{up} = 95%	Upwind Boundary n_{up} in Terms of D'_{shock} for P_{up} = 99%
CG at 2 AU	8×10^{26}	0.0006	21	85
CG at 1.3 AU	5×10^{27}	0.004	17	56
Borrelly	3×10^{28}	0.03	12	25
Halley	7×10^{29}	0.3	6	7
Hale-Bopp	1×10^{31}	1.5	2	3

[a]Note that the production rate Q is not the only factor that affects the shock distance, so for various solar wind conditions this Q is only a reference. Shock distance varies for different conditions; this table serves for the fact that for any comet whose shock distance is close to the ones listed, the certain minimum ratio nup should be used. CG is the short form for comet 67P/Churyumov-Gerasimenko.

purpose of the upwind boundary requirement determination, it is not necessary to be this accurate.

[78] The current uncertainties in absolute production rate measurements in comets are about 20% at best. Thus the error of current cometary simulations is tolerable below 5%. Figure B1 shows the difference between a larger comet and a smaller comet with different Qs: For the larger comet with a shock position $D_{shock} = 3 \times 10^5$ km, a boundary at $5D_{shock}$ is already including over 95% of the total mass loading. Yet for the smaller comet with $D_{shock} = 3 \times 10^4$ km, the upwind boundary needs to be over $10D_{shock}$ to include the same ratio of mass loading. Our numerical simulation confirms such estimations: for a Halley class comet with $D_{shock} = 3 \times 10^5$ km, the difference in steady state bow shock positions with an upwind boundary of 1.5×10^6 km ($n_{up} = 5$) from that of 4×10^6 km ($n_{up} = 13$) is less than 5%. For the case with a typical Jupiter family comet whose $D_{shock} = 3 \times 10^4$ km, such a difference in n_{up} results in the bow shock location difference of 10%. Unfortunately, the location of bow shock depends on the solar wind conditions as well, and there is no simple equation relates the production rate Q and the bow shock distance. Hence the only way to determine the appropriate boundary is to remain using the estimated D_{shock}.

[79] With the threshold of $P_{up} = 95\%$, we calculated the values for the minimum upwind boundary in the unit of shock distance. The solid curve in Figure B2 is the minimum upwind boundary position n_{up} plotted against the logarithm of shock distance D'_{shock} in unit of $\lambda_\infty = 10^6$ km. To make the estimation easier, we calculated a linear relationship which lies above the minimum in the realistic range. As shown in the dashed line of Figure B2, the relationship between the upwind boundary position n_{up} and the shock distance $D'_{shock} = D_{shock}/\lambda_\infty$ can be written as:

$$n_{up} = 17.6 - 5.73 \times [\log(D'_{shock}) + 2.63] \quad \text{(B3)}$$

Previous understandings described at the beginning of this section can be accordingly represented by $n_{up} = A \times D'_{shock}$, where A is an arbitrary factor usually set between 10 and 100. This empirical equation (B3) can serve as an improved estimation showing that this ratio n_{up} can be much smaller for larger comets than for smaller comets. To be more practical we list the typical factors in Table B1. From the calculations listed in the fourth column of Table B1, the n_{up} requirement for comet Halley is only 6 while for a smaller comet this should be as large as 20. This suggests that for a multiscaled model, simulation of larger comets requires less level of grid refinement than smaller comet simulation does. The typical requirements are listed in the fifth column of Table B1 for a more accurate simulation by including 99% of the upwind mass loading. It can be seen that compared with the previous approach we can safely shrink our calculation domain for the Halley case by a factor of 8 and still include over 99% of the mass loading. Boundary conditions for the sides and tail follow different requirements and are not covered by this study.

[80] **Acknowledgments.** The authors thank Dr. Ward B. Manchester IV, Dr. Darren L. De Zeeuw, Dr. Aaron Ridley, and Dr. Kenneth G. Powell for their help with the BATS-R-US model. The authors thank Dr. John Brandt and two anonymous reviewers for helpful comments which greatly improved the paper. Partial support for this work by NASA Planetary Atmospheres grant NNG05GP33G, NSF Planetary Astronomy grant AST 0098582, and NASA JPL Contract JPL 1266313 are gratefully acknowledged. Computer time on the NASA Ames Columbia system through award number SMD-06-0201 is also acknowledged.

[81] Amitava Bhattacharjee Gordon Holman and Rudolf Wegmann thanks for their assistance in evaluating this paper.

References

Barnard, E. E. (1920), On comet 1919b and on the rejection of a comet's tail, *Astrophys. J.*, *51*, 102.

Biermann, L. (1951), Kometschweife und solare Korpuskularstrahlung, *Z. Astrophys.*, *29*, 274.

Biermann, L., B. Brosowski, and H. U. Schmidt (1967), The interactions of the solar wind with a comet, *Sol. Phys.*, *1*, 254.

Bonev, T., and K. Jockers (1994), H_2O (+) ions in the inner plasma tail of Comet Austin 1990 V, *Icarus*, *107*(2), 335, doi:10.1006/icar.1994.1028.

Brandt, J. C. (1982), Observations and dynamics of plasma tails, in *Comets*, edited by L. L. Wilkening, pp. 519–537, The Univ. of Ariz. Press, Tucson.

Brandt, J. C., and R. D. Chapman (2004), Chapter 4: Introduction to comets, 2nd ed., Cambridge Univ, Press, New York.

Brandt, J. C., and M. Snow (2000), Heliospheric latitude variations of properties of cometary plasma tails: A test of the Ulysses comet watch paradigm, *Icarus*, *148*(1), 52.

Brandt, J. C., F. M. Caputo, J. T. Hoeksema, M. B. Niedner, Y. Yi, and M. Snow (1999), Disconnection events (DEs) in Halley's comet 1985–1986: The correlation with crossings of the heliospheric current sheet (HCS), *Icarus*, *137*, 69.

Brosius, J. W., G. D. Holman, M. B. Niedner, J. C. Brandt, J. A. Slavin, and E. J. Smith (1987), The cause of two plasma-tail disconnection events in comet P/Haley during the ICE-Halley radial period, *Astron. Astrophys.*, *187*(1–2), 267.

Combi, M. R. (2000), Hale-Bopp: What makes a big comet different? Coma dynamics: Observations and theory, *Earth Moon Planets*, *89*(1), 73.

Combi, M. R., and P. D. Feldman (1993), Water production rates in Comet P/Halley from IUE observations of H I Lyman-alpha, *Icarus*, *105*, 557.

Combi, M. R., W. M. Harris, and W. H. Smyth (2004), Gas dynamics and kinetics in the cometary coma: Theory and observations in Comets II, edited by M. C. Festou et al., pp. 523–552, Univ. of Ariz. Press, Tucson.

Fedder, J. A., S. H. Brecht, and J. G. Lyon (1984), MHD simulation of a comet magnetosphere, Memo, Rep. 5306, Nav. Res. Lab., Washington, D.C.

Forsyth, R. J., A. Balogh, E. J. Smith, and J. T. Gosling (1997), Ulysses observations of the northward extension of the heliospheric current sheet, *Geophys. Res. Lett.*, *24*(23), 3101–3104.

Galeev, A. A., F. V. Coroniti, and M. Ashour-Abdalla (1978), Explosive tearing mode reconnection in the magnetospheric tail, *Geophys. Res. Lett.*, *5*, 707.

Gombosi, T. I., D. L. De Zeeuw, R. M. Häberli, and K. G. Powell (1996), Three-dimensional multiscale MHD model of cometary plasma environments, *J. Geophys. Res.*, *101*(A7), 15,233.

Gombosi, T. I., K. C. Hansen, D. L. De Zeeuw, M.R. Combi, and K.G. Powell (1997), MHD simulation of comets: The plasma environment of comet Hale-Bopp, *Earth Moon Planets*, *79*(1), 179.

Haberli, R. M., M. R. Combi, T. I. Gombosi, D. L. De Zeeuw, and K. G. Powell (1997), Quantitative analysis of H_2O^+ coma images using a multiscale MHD model with detailed ion chemistry, *Icarus*, *130*(2), 373.

Keitch, G. S. (1986), The Giotto encounter with Halley's comet, *Br. Astron. Assoc. J.*, *96*(6), 328.

Konz, C., G. T. Birk, and H. Lesch (2004), Plasma-neutral gas simulations of reconnection events in cometary tails, *Astron. Astrophys.*, *415*, 791.

Niedner, M. B., Jr. (1981), Interplanetary gas: XXVI. A catalog of disconnection events in cometary plasma tails, *Astrophys. J. Suppl. Ser.*, *46*, 141–157.

Niedner, M. B., Jr. (1982), Interplanetary gas: XXVIII. A study of the three-dimensional properties of interplanetary sector boundaries using disconnection events in cometary plasma tails, *Astrophys. J. Suppl. Ser.*, *48*, 1–50.

Niedner, M. B., Jr., and J. C. Brandt (1978), Interplanetary gas: XXIII. Plasma tail disconnection events in comets: Evidence for magnetic field line reconnection at interplanetary sector boundaries?, *Astrophys. J.*, *223*, 655.

Niedner, M. B., Jr., and J. C. Brandt (1979), Interplanetary gas: XXIV. Are cometary plasma tail disconnections caused by sector boundary crossings or by encounters with high-speed streams?, *Astrophys. J. Part 1*, *234*, 723.

Ogino, T., R. J. Walker, and M. Ashour-Abdalla (1986), An MHD simulation of the interaction of the solar wind with the outflowing plasma from a comet, *Geophys. Res. Lett.*, *13*(9), 929–932.

Powell, K. G., P. L. Roe, J. L. Timur, T. I. Gombosi, and D. L. De Zeeuw (1999), A solution-adaptive upwind scheme for ideal magnetohydrodynamics, *J. Comp. Physiol.*, *154*, 284.

Rauer, H., R. Wegmann, H. U. Schmidt, and K. Jockers (1995), 3-D MHD simulations of the effect of comoving discontinuities in the solar wind on cometary plasma tails, *Astron. Astrophys.*, *295*(2), 529.

Russell, C. T., M. A. Saunders, J. L. Phillips, and J. A. Fedder (1986), Near-tail reconnection as the cause of cometary tail disconnections, *J. Geophys. Res.*, *91*(2), 1417–1423.

Russell, C. T., L. Guan, J. G. Luhmann, and J. A. Fedder (1989), The visual appearance of comets under varying solar wind conditions, *Adv. Space Res.*, *9*(3), 393–396(ISSN 0273-1177), doi:10.1016/0273-1177(89)90297-4.

Schmidt-Voigt, M. (1989), Time-dependent MHD simulations for cometary plasmas, *Astron. Astrophys.*, *210*, 433.

Smith, E. J., A. Balogh, R. J. Forsyth, and D. J. McComas (2001), Ulysses in the south polar cap at solar maximum: Heliospheric magnetic field, *Geophys. Res. Lett.*, *28*(22), 4159.

Snow, M., J. C. Brandt, Y. Yi, C. C. Petersen, and H. Mikuz (2004), Comet Hyakutake (C/1996 B2): Spectacular disconnection event and the latitudinal structure of the solar wind, *Planet. Space Sci.*, *52*, 313.

Spitzer, L. (1956), Physics of Fully Ionized Gases, Wiley-Interscience, Hoboken, N. J.

Tóth, G., et al. (2005), Space weather modeling framework: A new tool for the space science community, *J. Geophys. Res.*, *110*(A12), A12226, doi:10.1029/2005JA011126.

Villante, U., and R. Bruno (1982), Structure of current sheets in the sector boundaries: Helios 2 observations during early 1976, *J. Geophys. Res.*, *87*(A2), 607.

Voelzke, M. R. (2002), Disconnection events in comets, *Earth Moon Planets*, *90*(1), 405.

Voelzke, M. R. (2005), Disconnection events processes in cometary tails, *Earth Moon Planets*, *97*(3–4), 399.

Voelzke, M. R., and O. T. Matsuura (1998), Morphological analysis of the plasma structures of comet P/Halley, *Planet. Space Sci.*, *46*(8), 835.

Voelzke, M. R., and O. T. Matsuura (2000), The onsets of disconnection events of comet P/Halley on 1985 December 13–14 and 1986 February 22, *Astron. Astrophys. Suppl. Ser.*, *146*, 1.

Wegmann, R. (1995), MHD model calculations for the effect of interplanetary shocks on the plasma tail of a comet, *Astron. Astrophys.*, *294*(2), 601.

Wegmann, R. (2000), The effect of some solar wind disturbances on the plasma tail of a comet: Models and observations, *Astron. Astrophys.*, *358*, 759.

Wegmann, R., H. U. Schmidt, and T. Bonev (1996), The three-dimensional structure of the plasma tail of comet Austin 1990, *Astron. Astrophys.*, *306*, 638.

Yi, Y., J. C. Brandt, C. E. Randall, and M. Snow (1993), The disconnection events of 1986 April 13–18 and the cessation of plasma tail activity in comet Halley in 1986 May, *Astrophys. J.*, *414*(2), 883–891.

Yi, Y., J. C. Brandt, C. E. Randall, and M. Snow (1994a), The disconnection event of comet Halley on 1986 March 16.0, *Astron. J.*, *107*(4), 1591.

Yi, Y., F. M. Caputo, and J. C. Brandt (1994b), Disconnection events (DEs) and sector boundaries: The evidence from comet Halley 1985–1986, *Planet. Space Sci.*, *42*(9), 705.

Yi, Y., R. J. Walker, T. Ogino, and J. C. Brandt (1996), Global magnetohydrodynamic simulation of a comet crossing the heliospheric current sheet, *J. Geophys. Res.*, *101*(A12), 27,585.

M. R. Combi, T. I. Gombosi, K. C. Hansen, and Y.-D. Jia, Space Physics Research Laboratory, University of Michigan, AOSS, 1424C SRB, 2455 Hayward, Ann Arbor, MI 48109, USA. (yingdong@umich.edu)